Turbulent Methane Oxygen CFD Thermal Effects on Rotating Detonation Engine

Daniel Mendez

A thesis

submitted in partial fulfillment of the

requirements for the degree of

Master of Science in Aeronautics and Astronautics

University of Washington

2019

Reading Committee:

Carl Knowlen

Mitsuru Kurosaka

Program Authorized to Offer Degree:

Aeronautics and Astronautics

University of Washington

Abstract

Turbulent Methane Oxygen Combustion CFD Thermal Effects on Rotating Detonation Engine

Daniel Mendez

Chair of the Supervisory Committee:
Dr. Carl Knowlen
Aeronautics and Aeronautics

Thermal effects from Methane-Oxygen stoichiometric simulated heat of combustion in a turbulent annular rotating detonation engine (RDE) have been found to be manageable without the need of thermal management supporting subsystems under 1 second short pulse runs. Computer fluid dynamic simulations, using methane Lower Heating Value, show the current radially injected mixing design and copper & stainless-steel material choice to provide enough thermal management benefits. The transient and steady state thermal benefits of radially staggered injected fuel and oxidizer was explored in detail as well as the heat flux through walls and the overall dissipation of energy through conduction, convection, and radiation. Thermal management design improvements were also explored to increase the engine lifecycles.

TABLE OF CONTENTS

List of Figures iii

List of Tables v

Chapter 1. Introduction 1

1.1 Detonation Theory 2

1.2 RDE Operation 4

1.3 Thermodynamic Cycle 7

1.4 Heat Transfer Theory 8

1.5 Research Objectives 10

Chapter 2. Literature Review 11

2.1 Analytical RDE Research 11

2.2 CFD Turbulence & Thermal Solvers 18

2.3 Propulsion Engine Thermal Management Methods 20

Chapter 3. FSI Thermal Model CFD Configuration 26

3.1 3D Model Geometry 26

3.2 Mesh method and Mesh Quality 29

3.3 Fluent Model Configuration & Quantities Reports 34

3.3.1 Heat Source 34

3.3.2 General Solution 35

3.3.3 Boundary Conditions & Solvers 35

3.3.4 Mesh Sensitivity Analysis....37

Chapter 4. Results and Discussion....40

4.1 Results....40

4.1.1 Turbulence Model Results & Discussion....40

4.1.2 Thermal Model Results & Discussion....43

Chapter 5. Conclusion and Recommendations....56

5.1 Conclusion....56

5.2 Recommendation....57

Bibliography....58

LIST OF FIGURES

Figure 1. Propagating detonating shockwave inside a tube 1 D representation [3] 3
Figure 2. Hugonoit Curve, Rayleigh dashed lines, & strength identification [5]..... 4
Figure 3. RDE annular channel and reinforced detonation wave schematic [6]..... 5
Figure 4. University of Washington RDE short run valve actuation schedule [7]..... 6
Figure 5. General RDE detonation wave in annular region schemtic [8]..... 7
Figure 6. ZND pressure-volume diagram [9]..... 8
Figure 7. University of Washington RDE section cut view [11] 9
Figure 8. Azimuthal RDE shock-driven detonation methods of characteristics [9]..... 12
Figure 9. Azimuthal RDE shock-driven detonation turbulence thermal model [10] 12
Figure 10. Azimuthal shock-drive detonation regions [10] 13
Figure 11. Normal shock near a wall with oblique shock model [8]..... 14
Figure 12. inclined shock near a wall model [8] 16
Figure 13.Inclined shock near a wall model [8]..... 16
Figure 14. University of Washington radial injection scheme [15]..... 17
Figure 15. CFD solution of axially injected RDE [9]..... 17
Figure 16. heat management methods film cooling channels schematic [19] 21
Figure 17. General rocket nozzle film cooling system schematic [19]..... 22
Figure 18. Turbine blades cooling design schematic [21] 24
Figure 19. Turbine blades cooling design schematic [21] 24
Figure 20. University of Washington RDE section cut view [11]..... 26
Figure 21. RDE 3D model clay building method result 27
Figure 22. Resulting fluid geometry within the solid RDE geometry..... 28
Figure 23. RDE sectional view before meshing..... 29
Figure 24. RDE CFD fluid plenum mesh..... 30
Figure 25. RDE 90° section cut mesh..... 31
Figure 26. Partial RDE 90° section cut flow field mesh..... 31
Figure 27. Heat input volume..... 32

Figure 28. Detailed view of detonation plane, plenum, and surrounding solids mesh..... 33
Figure 29. Cutcell mesh flow field 38
Figure 30. Tetra Core mesh flow field..... 38
Figure 31. Right view turbulence solution at 0.5 seconds 40
Figure 32. Front view injection ports and mixing zone at 0.5 second..... 41
Figure 33. Methane-oxygen mixing through methane LHV heat input at 0.5 seconds.... 42
Figure 34. Lines used to gather temperature information..... 44
Figure 35 Line 1 Temperature profile at 1 second 45
Figure 36 Line 2 Temperature profile at 1 second 45
Figure 37 Line 3 Temperature profile at 1 second 46
Figure 38 Line 4 Temperature profile at 1 second 46
Figure 39 Inner and Outer Cylinder temperature propagation at 0.5 seconds 47
Figure 40 Inner and Outer Cylinder temperature propagation at 1 second..... 48
Figure 41 Outer Sleeve temperature propagation at 0.5 seconds 49
Figure 42 Outer Sleeve temperature propagation at 1 second..... 49
Figure 43 Front Plate and Injection Rings temperature propagation at 0.5 seconds 50
Figure 44 Front Plate and Injection Rings temperature propagation at 1 second 51
Figure 45 Inner and Outer Injection Ring temperature profile at1 second 51
Figure 46 Inner and outer ring temperature contour & methane mass fraction contour between injection rings at 1 second 52
Figure 47 Largest temperature seen per component at 1 second..... 54

LIST OF TABLES

Table 1. Mesh cell size and statistical parameters 34
Table 2. Mesh inflation parameters 34
Table 3. Mesh analysis results 39
Table 4 Energy Balance 55

ACKNOWLEDGEMENTS

The author is grateful for the financial support provided by The Boeing Co., for the family-like atmosphere within the William E. Boeing Department of Aeronautics and Astronautics that was made possible by the exceptionally talented and genuinely good human beings that are the students and staff. He is grateful for his research advisors Carl Knowlen and Mitsuru Kurosaka who opened the doors to join the University of Washington Rotating Detonation Engine (UWRDE) team. The members of the team – Jacob A. Boening, Eric A. Wheeler, Kevin Chau, Lien Chang, and especially James Koch – whom all somehow positively affected or supported the author from orientation day until graduation day. The high-power computing IT support from Stephen T. Scheier. The outside mentorship in The Boeing Co. Thermal Analysis team from Michael T. Dunn and Hin-Fan M. Lau in thermal analysis and computational fluid dynamics (CFD) and work colleague at Boeing Rohan S. Sharma in CFD. Professors that inspired the author while taking their classes, Mark Kot from the Applied Mathematics dept., the happiest mathematician, and Robert Breidenthal from the Aeronautics and Astronautics dept., the professor that made turbulence practical while telling a joke or two.

DEDICATION

To my parents, Angela M. Vasquez and William F. Mendez,

for you are my inspiration as the manifestation of dedication

and most importantly

a good laugh

Thank you

Chapter 1. INTRODUCTION

The rotation detonation engine (RDE) is emerging as the next step beyond the pulse detonation engines (PDE). The PDE is based on a self-aspirating operation which is inherently unsteady due to fuel injecting taking place between detonations. It requires unsteady gas dynamic calculations to determine pressure output and integration over a cycle to determine performance. The PDE deflagration-to-detonation (DDT) process also requires a longer channel in comparison to the RDE [1]. The PDE method offers an approximation to the continuous detonation that the RDE offers, making RDE the forefront in propulsion technology. The RDE offers higher thermodynamic efficiencies and higher mass flux while providing a more stable propulsion. RDE technology is being developed at a scale that is more easily implemented in rocket propulsion; however, it will also aid aircraft propulsion and powerplant energy production when correctly configured within the respective thermodynamic cycles. Just like other aircraft engines, material heating limits are known to influence product deign to a high degree if the product has to deal heat whether the heat is internal or external to the product. Exposure to thermal environments may produce thermal fatigue related structural failure such as material deformation and/or cavitation. Two parallel paths of innovation work together towards decreasing material design heating limits. One path is paved by the material sciences field pursuing the creation of new elements and designing material structures that can withstand higher temperatures by dissipating heat more efficiently. The second parallel path is the innovation of thermal management systems. From the fan in a computer to the water circulation system in astronaut suits, these systems work to manage heat transfer to prologue the life cycle of the product's mission. Herein is presented a "strong" fluid structure interaction (FSI) analysis to explore the detonation wave thermal conduction and convection effects on the

engine. A “strong” FSI analysis is based on an all-encompassing code that uses CFD to determine the internal flow field in the injector region of the RDE and its effect on engine structure through a simultaneous finite element method (FEM) analysis with a mesh where all nodes are connected and continuous throughout. A “weak” FSI analysis splits the CFD analysis from the structure FEM analysis by first solving for the fluid behavior and implementing the results onto the structure separately [2]. The turbulent CFD analysis explored herein is based on the ANSYS Fluent SST *k-w* solver in combination with the Intermittency Transition model. Efficiency improvements offered by the RDE aid in more efficient fuel consumption; however, the implementation of this technology in aircraft engines and powerplants provides additional benefits. Replacing the compression and combustion sections of an engine with an RDE means that there is no need for a compression section with rotating blades and stationary veins; therefore, decreasing the weight of the engine and decreasing the number of moving parts. These improvements translate to an improvement in aircraft weight economy and a decrease in maintenance costs in addition to the fuel consumption efficiency improvements.

1.1 Detonation Theory

The fundamental detonation event behind the RDE can be illustrated with a propagating detonation wave in a tube. Figure 1 [3] shows a shockwave traveling in a positive x-direction as it consumes unburned reactants; resulting in a combustion-drive shock that is the essence of a detonation wave. Because the shock is moving at supersonic speeds the unburned fuel and oxygen are unaware of its approach, so these are stagnant until the shock moves across unconsumed reactants now placing reactants in the Reaction Zone. The compression and temperature rise across the shockwave initiates combustion, which releases heat that couples with the wave to enable it to be self-sustaining as it continuously propagates.

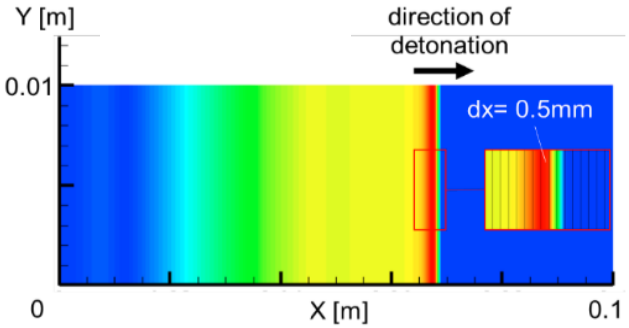

Figure 1. Propagating detonating shockwave inside a tube 1 D representation [3]

This detonation wave process is idealized with the ZND model (after Zeldovich, von Neumann, and Döring) that assumes a one-dimensional flow, a jump discontinuity across the shockwave, and an emerging material behind the shock that is in thermochemical equilibrium at the thermally choked condition relative to the shockwave. The following are the conservation laws of Mass (Eqn. 1), Momentum (Eqn. 2), and Energy (Eqn. 3) behind the model where state 1 represents the burned zone behind the shock and state 2 represents the unburned zone forward of the shock. [4]

$$\rho_1 u_1 = \rho_2 u_2 \tag{1}$$

$$p_1 + \rho_1 {u_1}^2 = p_2 + \rho_2 {u_2}^2 \tag{2}$$

$$h_1 + \frac{{u_1}^2}{2} + q = h_2 + \frac{{u_2}^2}{2} \tag{3}$$

By substituting Eqn. 1 into Eqn. 2 we obtain what is called the Rayleigh (Eqn. 4) line which is a function of *p-v*. It enables the use of the relationship in term of only one of the velocities u. Here, v represents specific volume.

$$p_2 - p_1 = {u_1}^2 {\rho_1}^2 \left(\frac{1}{\rho_1} - \frac{1}{\rho_2}\right) = \frac{{u_1}^2}{{v_2}^2}(v_1 - v_2) \tag{4}$$

Likewise, substituting by Eqn. 4 into Eqn. 3 we again eliminate a velocity *u* and obtain the Hugonoit relationship (Eqn. 5) also in the *p-v* plane. The tangential intersection between the

Rayleigh line and the Hugonoit curve provide the state for a detonation velocity that satisfy the jump conditions [5].

$$h_2 - h_1 = (p_2 - p_1)\frac{v_1 + v_2}{2} - q \tag{5}$$

Per Figure 2 [5], the point at which a Rayleigh line is tangent to the Hugonoit curve helps define the strength of the detonation.

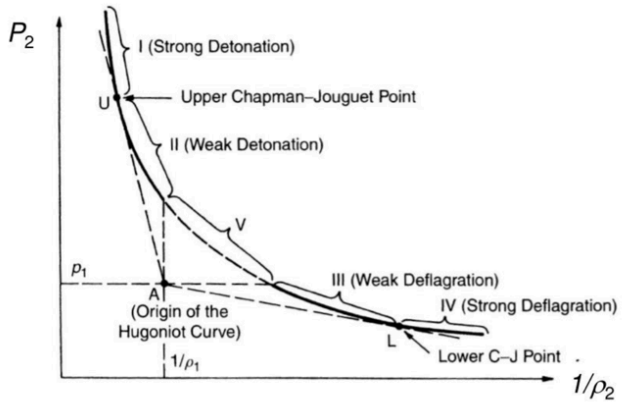

Figure 2. Hugonoit Curve, Rayleigh dashed lines, & strength identification [5]

1.2 RDE OPERATION

It is well understood in academia that the ZND model for detonation (section 1.1) shockwave detonation in a tube serves as the fundamental building block behind the RDE and other detonation based thermodynamic cycles. The application of shockwave detonation in a tube can be simply applied by connecting the ends of the tube, forming a circular channel. An RDE shockwave is initiated by igniting a sequence of spark plugs in the reactant filled plenum. The spark plug sequence reinforces the detonation wave to travel in one unique direction. The shockwave continues to travel through the circular channel until it has consumed all reactants that continue to

reinforce the shockwave. This revolution then continues if the reactants are continuously introduced into the detonation plenum. The three-dimensional view of said circular channel can be represented with an annular circular prism. A simple RDE geometry consists of two concentric cylinders with space in between the cylinders. The space is the volume in which detonation takes place and the reinforcement of said detonation waves can be seen in Figure 3. [6]

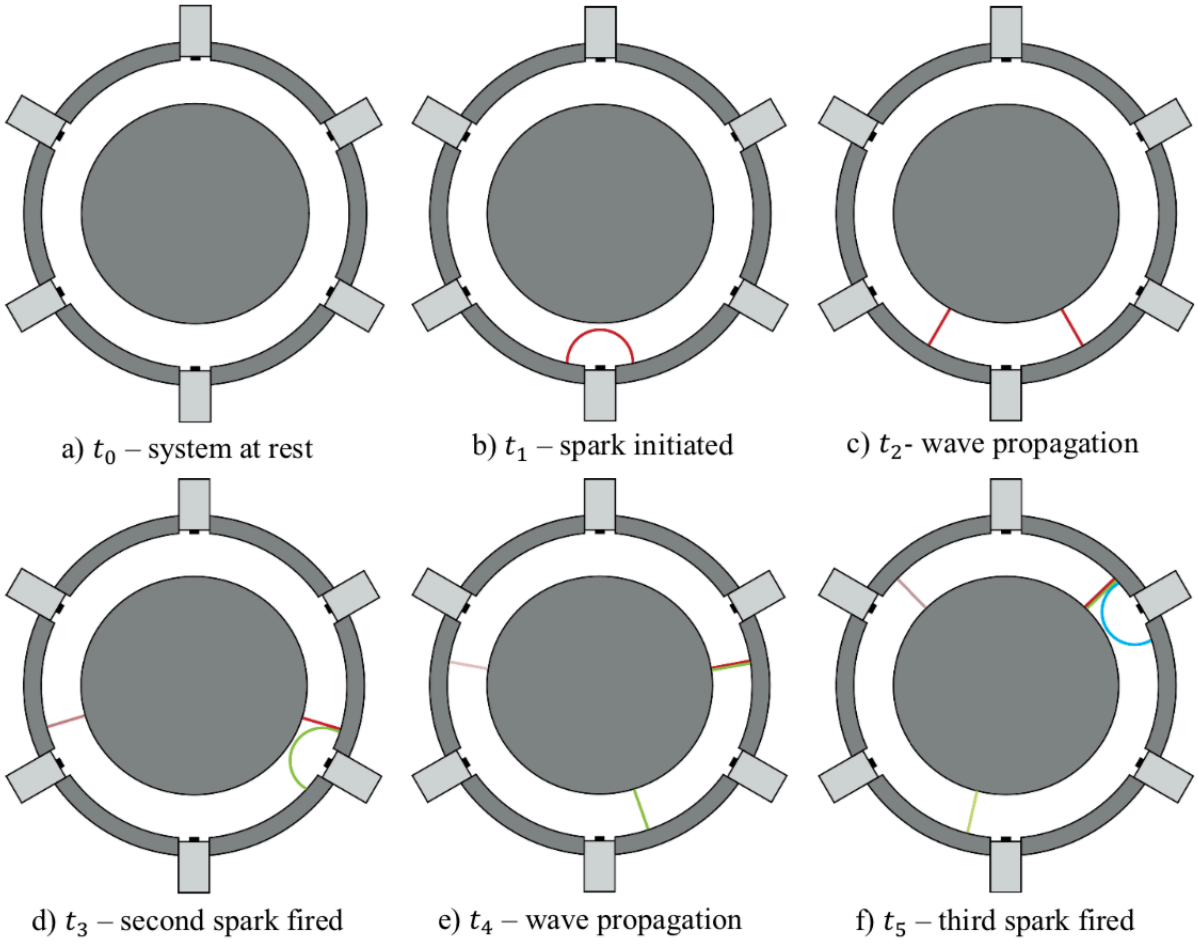

Figure 3. RDE annular channel and reinforced detonation wave schematic [6]

The experimental operation of the RDE at the University of Washington followed a procedure that commences by injecting ignition prevention nitrogen gas. Per Figure 4, the spark plug sequence initiates before the nitrogen finalizes injection to prove that enough nitrogen is diluting the plenum and the detonation ignition will take place only when the reactants are injected. After the nitrogen stops flowing the fuel and oxygen as then injected while the sparks continue to ignite in one direction. After the reactants stop flowing the system is then again injected with nitrogen to terminate the experimental sequence [7].

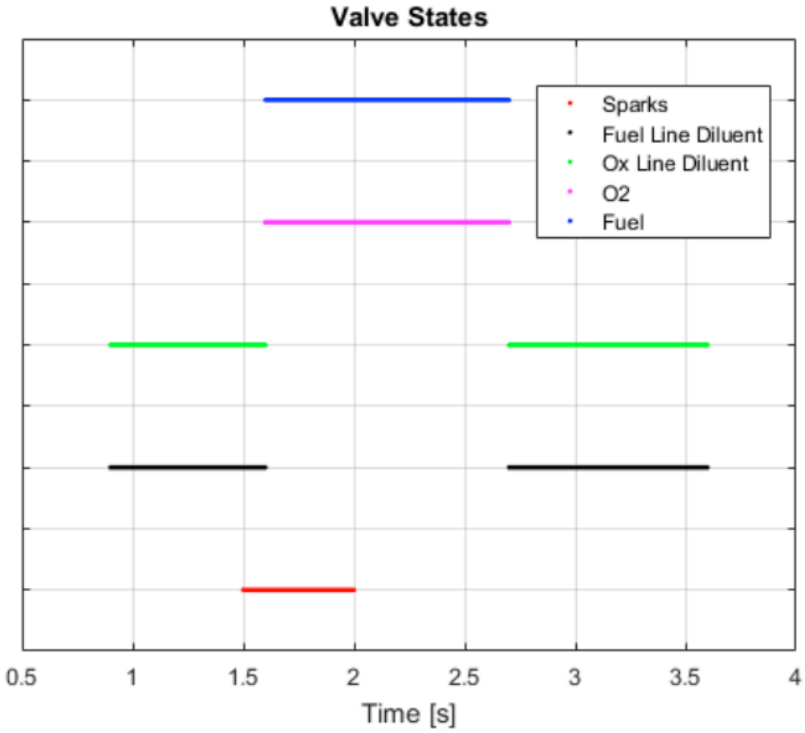

Figure 4. University of Washington RDE short run valve actuation schedule [7]

Figure 5 is a schematic representation of how the detonation wave behaves as it travels through the annular space, which will be analyzed more in depth in section 2.1 of this thesis. [8]

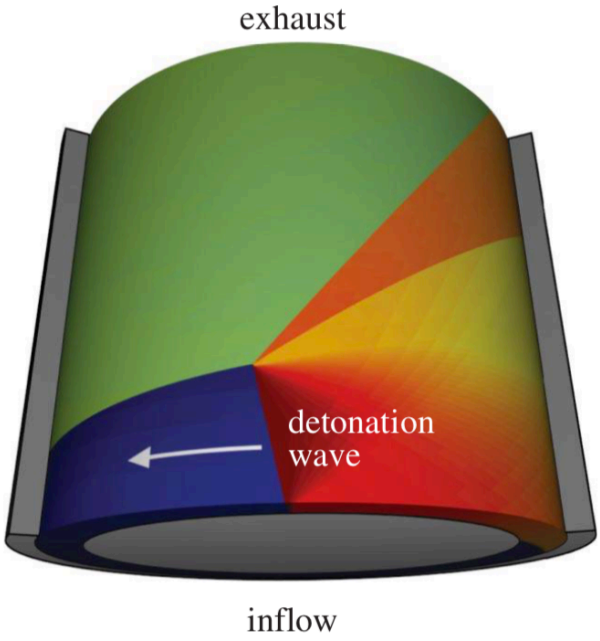

Figure 5. General RDE detonation wave in annular region schemtic [8]

1.3 THERMODYNAMIC CYCLE

From the previous section 1.1 it's understood that the conventional thermodynamic cycle *P*-*v* diagram can be gathered from the Rayleigh and Hugonoit curves with the exception that a pressure curve must be accounted, which would be a constant pressure line. Figure 6 [9] shows the *P*-*v* diagram describing the thermodynamic cycle of an RDE. Detonation starts at the Upstream initial conditions, creating an increase in pressure and temperature across the shock. Subsequently heat is added through the subsonic Rayleigh process and ends at the tangential intersection between the Rayleigh and Hugonoit curves, the Chapman-Jouguet (CJ) limit. The CJ point corresponds to the

minimum propagating velocity and maximum entropy along the Rayleigh process line, thus equilibrium is achieved.

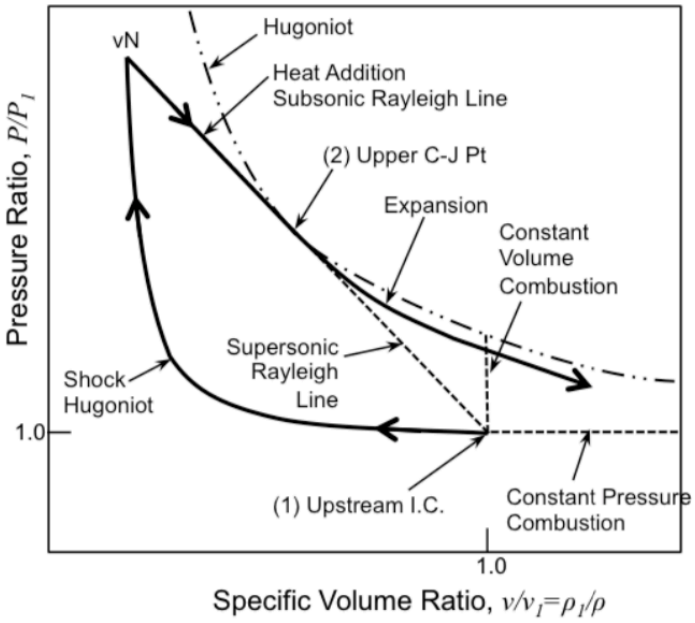

Figure 6. ZND pressure-volume diagram [9]

1.4 HEAT TRANSFER THEORY

Just like airplane, rocket, and powerplant engines, the RDE is an engine that must withstand high thermal loads that can cause thermal fatigue related failures on engine structure. Per Figure 7, the RDE design discussed herein uses copper in the inner and outer combustion adjacent cores and stainless steel in the front plate and outer shell.

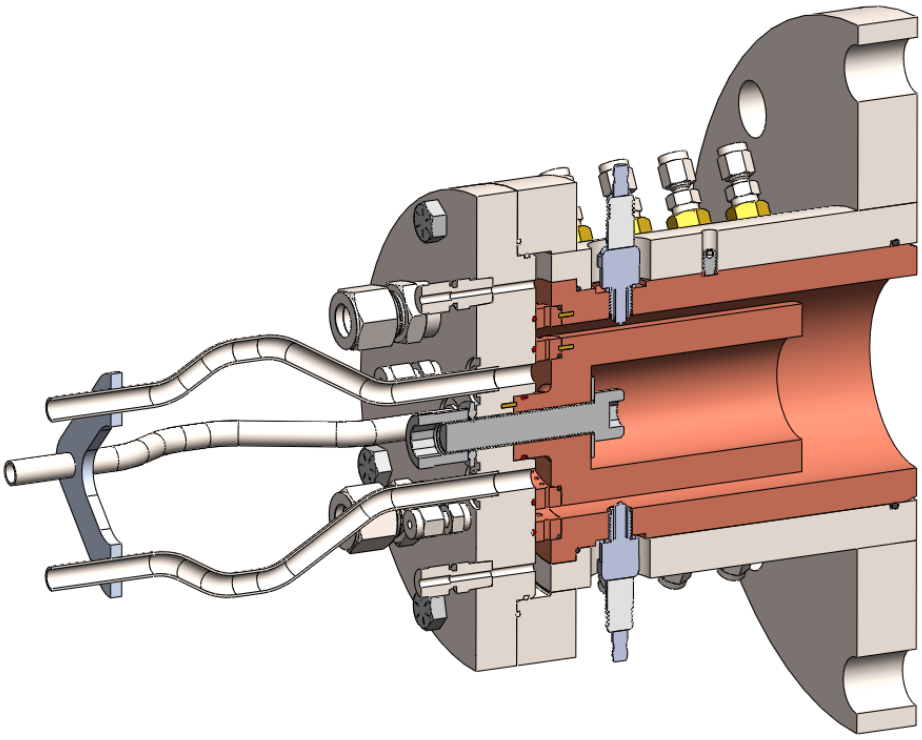

Figure 7. University of Washington RDE section cut view [11]

Inside the fluid the conductive heat transfer is modeled through the transient heat conduction Eqn.6 shown here in its most general form, where k is the material conductivity, q_v is the rate at which energy is generated per unit volume of the medium, ρ is the density, ϕ is the radial angle, and c_p is the specific heat capacity. Moreover, the convective heat transfer analysis takes the conductive boundary conditions to model the thermal effects on the structure through transient conductive heat transfer Eqn. 7 shown here in cylindrical coordinates [11], where θ is temperature, t is time, r is radius, and α is thermal diffusivity. [12]

$$\frac{1}{r}\frac{\partial}{\partial r}\left(kr\frac{\partial\theta}{\partial r}\right)+\frac{1}{r^2}\frac{\partial}{\partial\phi}\left(kr\frac{\partial\theta}{\partial\phi}\right)+\frac{\partial}{\partial z}\left(k\frac{\partial\theta}{\partial\phi}\right)+q_v=\rho c_p\frac{\partial\theta}{\partial t} \quad (6)$$

$$\frac{\partial\theta}{\partial t}=\alpha\left(\frac{\partial^2\theta}{\partial r^2}+\frac{1}{r}\frac{\partial\theta}{\partial r}\right) \quad (7)$$

These transient equations are fully functional and will be used through ANSYS Fluent analysis tool as an industry accepted simulation code. ANSYS heat transfer verification and validation CFD cases are public and one is referenced here for the reader's convenience. [13]

1.5 Research Objectives

To help further the understanding of the RDE detonation impact on its structure a single phase turbulent thermal model was created to analyze heat conduction, convection, and radiation. Results from the research helps further understand axial location of detonation, radially injected reactants turbulence mixing effects, and the thermal benefits and risks that these impose on the specific engine design being analyzed herein.

Chapter 2. LITERATURE REVIEW

This section is dedicated to exploring past and current research in support of the knowledge presented in this thesis. Past and current knowledge pertaining to PDE, RDE, and FSI research and its understanding must be treated as fundamental. The pursuit of knowledge is noble when it indeed moves innovation forward to improve the human condition.

2.1 ANALYTICAL RDE RESEARCH

Extensive investigation has been conducted throughout academia in regard to the numerical methods that approach physical values and visual representations of the RDE. These numerical models have focused in geometry representation and flow conditions as well as varying pressure conditions upstream and downstream of the detonation plenum. These, following the detonation cycle, find that losses occur where reactants are burned away from the detonation wave additional to losses when detonated reactants are forced through the oblique and secondary shockwaves. Schwer and Kailasanath et al. consistently calculated less than 10% efficiency loss when reactants meet the burned gases meet due through the shockwaves due to premixed gases burning [14]. A visual representation that begins to shape the 2-D numerical modeling of the RDE is beautifully depicted by Fievisohn and Yu in Figure 8 [9]. Their method of characteristics (MOC) approach show a 2-D unfolded representation of the cylindrical detonation shockwave resulting from a two-wave solution. One advantage for employment of MOC and other numerical methods is the computational cost economy these offer. However, these may require more care in boundary condition definitions, chemical reactions, and frame of reference.

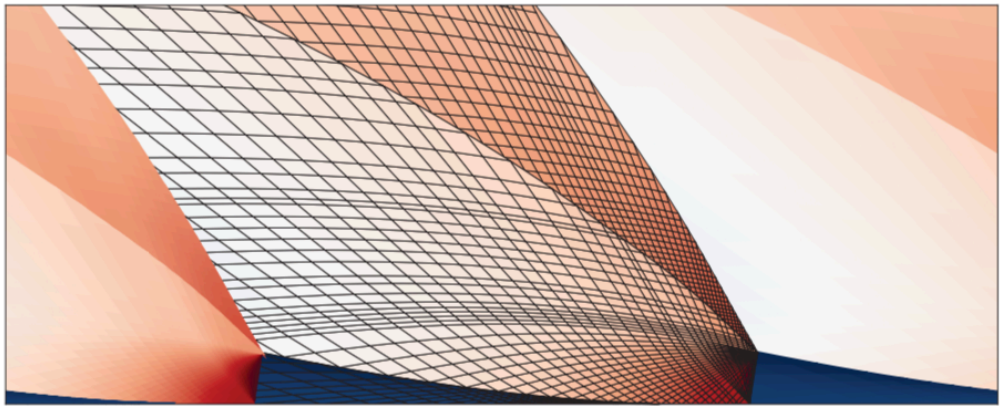

Figure 8. Azimuthal RDE shock-driven detonation methods of characteristics [9]

Additional development in the visual flow field representation can be seen in Figure 9, where Nordeen shows a single-step snapshot of the 2-D time-accurate numerical solution [9]. The intentional exaggeration of the contour map helps define predictions of how high temperature may reach as well as the geometrical flow characteristics.

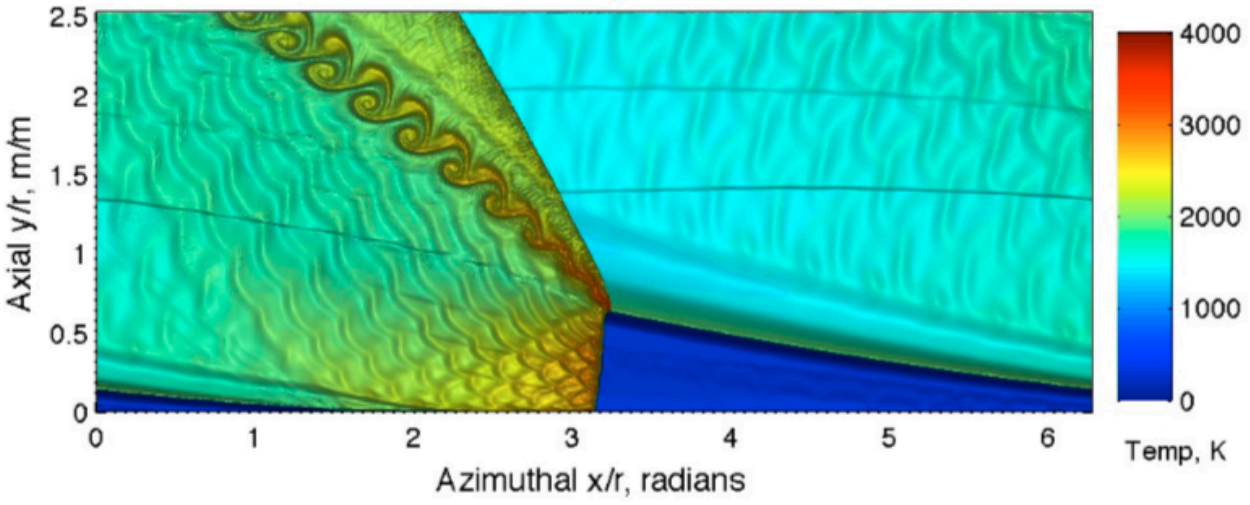

Figure 9. Azimuthal RDE shock-driven detonation turbulence thermal model [10]

Nordeen also helps explain the zones that this steady state solution communicates through Figure 10. It is advantageous however to recognize in Figure 10 that the “Expansion Flow to Exhaust Plane” region contains a secondary shockwave in between the “Vortex Train and Shear Layer”

and the “Recovery Flow” zones. This recognition helps to visually identify the region where some efficiency loss takes place, as explained earlier in this section with Schwer’s and Kailasanath’s et al findings.

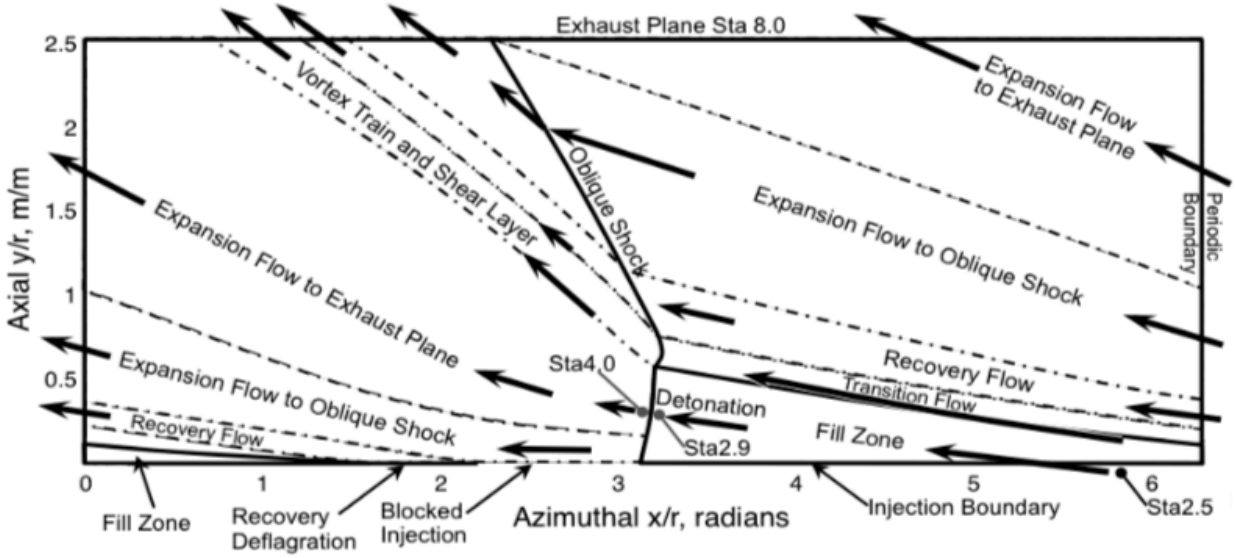

Figure 10. Azimuthal shock-drive detonation regions [10]

By qualitatively inspecting flow fields the motivation to understand the numerical calculation of the RDE flow field geometry, pressure, and temperature profiles, amongst others, is now established. A common denominator among these numerical methods is the foundation detonation oblique shockwave geometry which is the result of a modified ZND model. Figure 11 shows an idealized normal shockwave with a wall and an expansion fan coming the oblique shockwave portion [8]. This model serves as a reference foundation to determine flow geometry through isentropic shockwave relations.

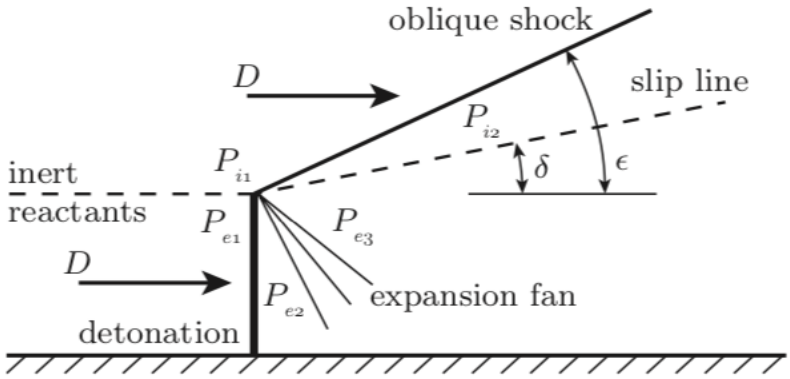

Figure 11. Normal shock near a wall with oblique shock model [8]

It shows an idealized normal shockwave with a wall and an expansion fan coming the oblique shockwave portion [8] where subscript *e* stands for explosive mixture and subscript *i* stands for inert bounding gas. The normal shockwave acts as an object that creates both the compression oblique shockwave and expansion fan due to its reference to the flow. Pressure rise across the normal shockwave is larger than the pressure rises across the oblique shockwave, however there is a region behind the expansion fan that is at same pressure behind the oblique shock; therefore, $P_{e3} = P_{i2}$. Additionally, knowing the CJ model provides value for both *D* and P_{e2} are known. The following oblique shockwave isentropic relations describe the relationship between the different portions of the idealized flow field.

$$\tan(\delta) = 2\cot(\epsilon)\left[\frac{{M_{i1}}^2 sin^2(\epsilon) - 1}{{M_{i1}}^2(\gamma_i + \cos(2\epsilon)) + 2}\right] \tag{8}$$

$$\delta = \nu(M_{e3}) - \nu(M_{e2}) \tag{9}$$

Here Eqn. 9 is founded on the fan flow Prandtl-Meyer function. Equations 10, 11, and 12 provide the isentropic pressure rise across the oblique shockwave, normal shockwave, and their relating pressure ratios, respectively.

$$\frac{P_{i2}}{P_{i1}} = 1 + \frac{2\gamma_i}{\gamma_i + 1}\left({M_{i1}}^2 sin^2(\epsilon) - 1\right) \tag{10}$$

$$\frac{P_{e2}}{P_{e3}} = \left[\frac{1 + \left[\frac{\gamma_{e2} - 1}{2}\right]{M_{e3}}^2}{1 + \left[\frac{\gamma_{e2} - 1}{2}\right]{M_{e2}}^2}\right]^{\gamma_{e2}/(\gamma_{e2}-1)} \tag{11}$$

$$\frac{P_{i2}}{P_{i1}} = \left(\frac{P_{e1}}{P_{i1}}\right)\left(\frac{P_{e2}}{P_{e1}}\right)\left(\frac{P_{e3}}{P_{e2}}\right) \tag{12}$$

However, it is established early in this thesis that there is continuous injection of reactants (or explosive mixture as referred to in this section) in front of the shockwave so that it may consume the reactants and propel the shockwave. The injection of this could impact the shape of the shockwave to different degrees. Injection schemes were reactants are injected perpendicular to the structure wall introduce a velocity vector parallel to what is currently the normal shockwave portion of the flow field. As the normal shockwave travels along the wall the consumed gas flows downstream of the shockwave as it expands. The expanding gases and the new reactants being injected meet in space gradually turning the injection velocity vector clockwise. The injection velocity vector turned clockwise creates a different flow for the incoming normal shockwave. The normal shockwave will rotate such that the shockwave is normal to the combined expansion fan flow and reactant injection vector, as shown in Figure 12.

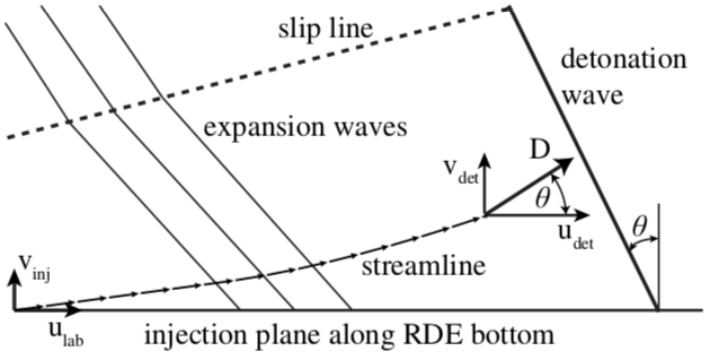

Figure 12. inclined shock near a wall model [8]

The resulting shockwave configuration in reference to the horizontal wall is depicted by Figure 13 below.

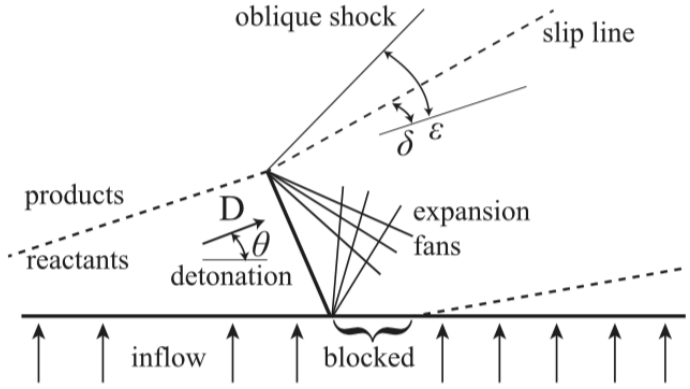

Figure 13.Inclined shock near a wall model [8]

The three-dimensional representation of the shockwave's inclination is existent in all annular region RDE deigns independent on the injection scheme's geometry relative to the supersonic flow. The University of Washington RDE design injects radially staggering oxygen-fuel injection ports that create entrainment regions as depicted in Figure 14.

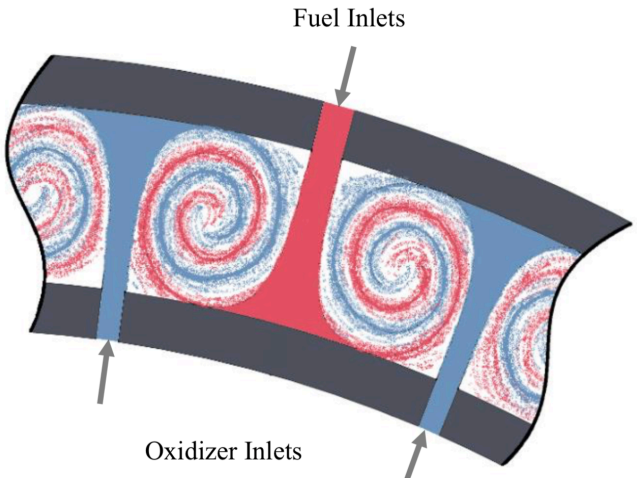

Figure 14. University of Washington radial injection scheme [15]

This injection scheme doesn't directly affect the inclination of the shockwave. The shockwave however is being created downstream of the injection region; therefore, the mass flow rate is still traveling radially and having a secondary effect on the inclination of the shockwave. This concludes exploration in the basics of the shockwave geometry and how it is being modeled in academia. Finally, Figure 15 shows a computer fluid dynamics model solution of the RDE as depicted by Nordeen's work [9].

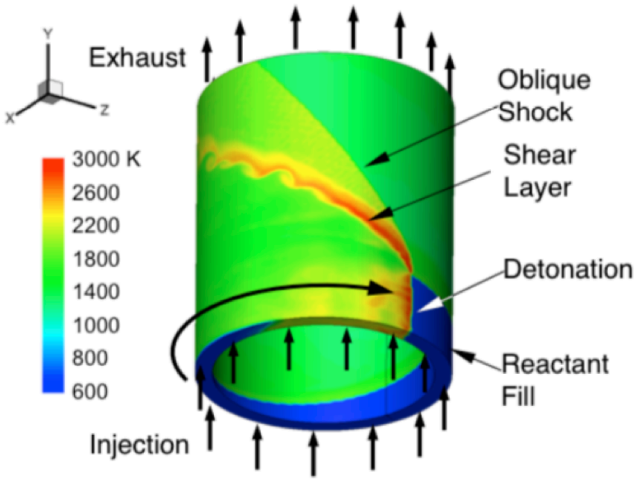

Figure 15. CFD solution of axially injected RDE [9]

2.2 CFD TURBULENCE & THERMAL SOLVERS

The Fluid Structure Interface (FSI) analysis method implemented herein uses the ANSYS Fluent industry accepted computer fluid dynamics (CFD) solvers; therefore, only CFD methods will be explored in this section to support an appropriate analysis. Per the analysis intention, only non-reacting flow research was considered. The motivation for an FSI stems from the need to identify the failure of heating components due to high temperature and thermal fatigue failure because of excessive temperature gradient and thermal stress. Therefore; it is paramount to identify the relevant analytical relationships that the CFD codes rely on. It is understood that heat is transferred through conduction, between fluids, and through convection, between a solid and a fluid. Conduction can be modeled by the three-dimensional Fourier's law in cartesian coordinates per Eqn. 13. Here $\dot{q}$ expresses heat flux per unit area in $\frac{J}{sm^2}$, T is the change in temperature, and k is the heat transfer coefficient [16].

$$\dot{q} = -k\frac{dT}{dx}\frac{dT}{dy}\frac{dT}{dz} \tag{13}$$

The convection phenomenon is dependent on the fluid and solid, so it is necessary to examine features of the fluid motion near a surface. If the fluid is uniformly hotter than the solid, the boundary layer of the fluid will carry most of the temperature difference between the fluid and the solid. The thickness of the boundary layer is dependent on the Reynolds Number, structure of the wall surface, pressure gradient, and Mach number. The convection formula must then be dependent on the temperature difference, the boundary layer, and the heat transfer coefficient. The boundary layer, δ, and the heat transfer coefficient, k, are both taken into account in Eqn. 14 and known as the Convective Heat Transfer Coefficient, h in $\frac{J}{sm^2K}$ [17].

$$h = \frac{k}{\delta} \tag{14}$$

Subsequently, the heat flux per unit area due to convection is defined by Eqn. 15 using Eqn. 14 and it is known as Newton's Law of Cooling. Here T_w represents the temperature at the wall and T_∞ represents the temperature in the fluid.

$$\dot{q} = \frac{\dot{Q}}{A} = h(T_w - T_\infty) \tag{15}$$

Both, the convection and conduction problems, define a clear horizon on the Fluid Structure interface (FSI) model being pursued in this thesis. However, the conduction problem must be further explored due to the nature of the RDE fluid in motion. The fluid does not have one uniform temperature so the conduction problem can be modeled with Eqn. 14 but it must rely on the transport theorems to model laminar flow, laminar to turbulence transition, and turbulence to help identify the direction of the flow throughout the volume as the heat is added by detonation and how turbulence may affect the heat throughout the fluid, consequently transferring heat onto the structure through convection. Entrainment zones, zones where the flow is turbulent and well mixed, will carry more heat more so than un-entrained flow. Referring back to Figure 7 shows how the vortex train and shear layer carry higher heat than the surrounding non-turbulent fluid. The transition between laminar and turbulent flow is therefore very important and are defined by Eqn. 16 and Eqn. 17, the Navier-Stokes equations of incompressible fluid for laminar and turbulent flows, respectively. Here τ_t is the turbulent stress tensor.

$$\rho\left(\frac{\partial u}{\partial t} + u * \nabla u\right) = \nabla p + \mu\nabla^2 u \tag{16}$$

$$\rho\left(\frac{\partial u}{\partial t} + u * \nabla u\right) = \nabla p + \mu\nabla^2 u + \nabla * \tau_t \tag{17}$$

For this reason the Transition SST ANSYS solver was explored; however, after thorough analysis it was not chosen. The solver uses the shear stress *k-w* transport equations and couples these with the intermittency transport and the transition onset criteria transport equation, in terms of momentum-thickness Reynolds number. The solver is trusted per the empirical correlation [17] provided by ANSYS for the bypass transition; however, it has limitations that were accounted for and one of these was deemed relevant to change the solver for the analysis in this thesis. The Transition SST model is only applicable to wall-bounded flows, it should not be applied in analysis where a surface moves relative to the coordinate system, should be applied in flows with a defined nonzero freestream velocity so it should not be applied in wall jet flows. Since the RDE model injects the reactants like a wall jet flow the Shear Stress (SST) *k-w* model was chosen with the Intermittency Transition model enabled as recommended by the ANSYS user manual. It must be understood that the solver has not been calibrated in combination with buoyancy and multiphase turbulence physical effects, so these will not be analyzed in this thesis. The SST *k-w* model accounts for the transport of turbulent shear stress in the definition of turbulent viscosity which makes the model more accurate than others and more reliable in adverse pressure gradient flows, airfoils, and most importantly on transonic shockwaves. The additional Intermittency solver applied aids with the transport equation for turbulence intermittency. [18]

2.3 Propulsion Engine Thermal Management Methods

As a result of detonation, it is desirable to understand the mechanical effects on the structure. One of the most relevant applications of this understanding is in the thermal management designs on rocket engines. Some current rocket boosters presently use film cooling strategies in combination

with strategic material choice. One of the boosters used in the satellite launch vehicle ISRO is designed as a double-walled construction, as shown in Figure 16.

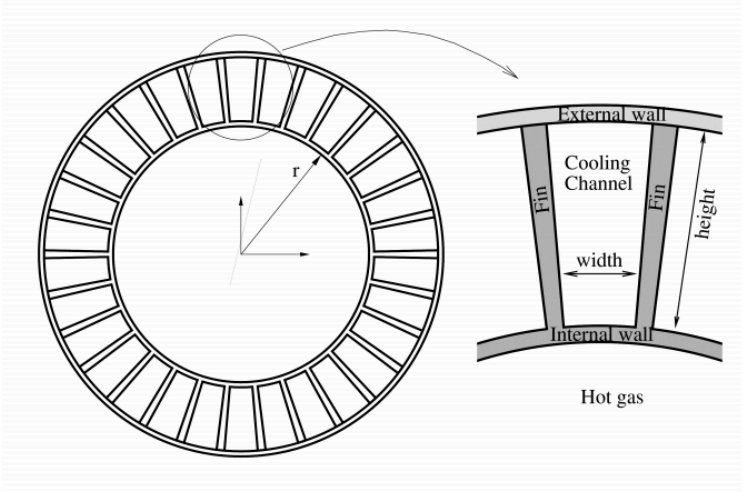

Figure 16. heat management methods film cooling channels schematic [19]

The inner wall is made of copper while the outer wall is stainless steel and in between a regenerative cooling chamber encaged by rectangular channels that are milled onto the surface of the inner wall. Per Figure 17, fuel is pumped through the cooling channel before it reached the combustion chamber to mix with the oxidizer.

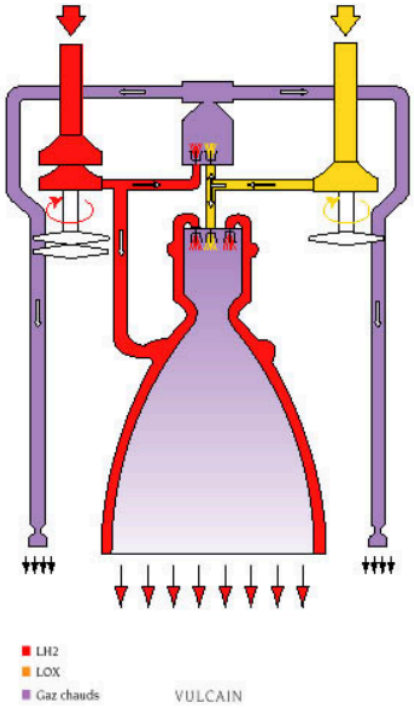

Figure 17. General rocket nozzle film cooling system schematic [19]

The motive behind this conventional booster cooling design is based on the obstacles set by low cycle fatigue, thermal ratcheting, and creep. Low cycle fatigue (LCF) is the reciprocal of the number of cycles to fatigue failure and is numerically identified as D_{LCF} per Eqn. 18. Here N_f is the number of cycles to fatigue failure at the highest operating temperature, as defined by Asraf et al [20].

$$D_{LCF} = \frac{1}{N_f} \tag{18}$$

Per Eqn. 19, ratcheting damage is the ratio of accumulated plastic tensile strain in a cycle to the fracture strain of the material.

$$D_{rachetting} = \frac{\varepsilon_{acc}}{\varepsilon_f} \tag{19}$$

And per Eqn. 20, creep is the ratio of time of operation to time to failure by creep at a unique stress level.

$$D_{creep} = \left(\frac{t}{t_f}\right)_{\sigma} \quad (20)$$

The addition of Eqn. 18, 19, and 20 provide the total damage. Thereafter, Eqn. 21 can be derived to provide a definition for N_f as a function of D_{total}.

$$D_{total} = D_{LCF} + D_{rachetting} + D_{creep} \quad (20)$$

$$N_f = \frac{1}{D_{total}} \quad (21)$$

Asraff et al concluded from their analysis that creep has insignificant effects on stainless steel and that low cycle fatigue (LCF) is rather the main cause for the inner wall copper mechanical failures. LCF is the result of low number of cycles at a stress level that causes plastic deformation. The transition from elastic to plastic deformation is dependent on the material ductility, copper in this case. Therefore, the determination whether the RDE design is LCF or high cycle fatigue (HCF) is dependent on how many cycles are required before a material rupture.

Another approach of engine thermal management methods is provided by the conventional turbofan engine in most commercial airplanes. One example within the engine may be identified when high-pressure compressor section bleed air is used to cool down the structure around the high-pressure turbine section. However, an even smaller detailed temperature management method is seen when low-pressure and high-pressure air is channeled through the inside of turbine vanes to cool them. Figure 18 and Figure 19 show a sectional view of an internal cooling system and the sectional view of a vane and its cooling channels, respectively [21].

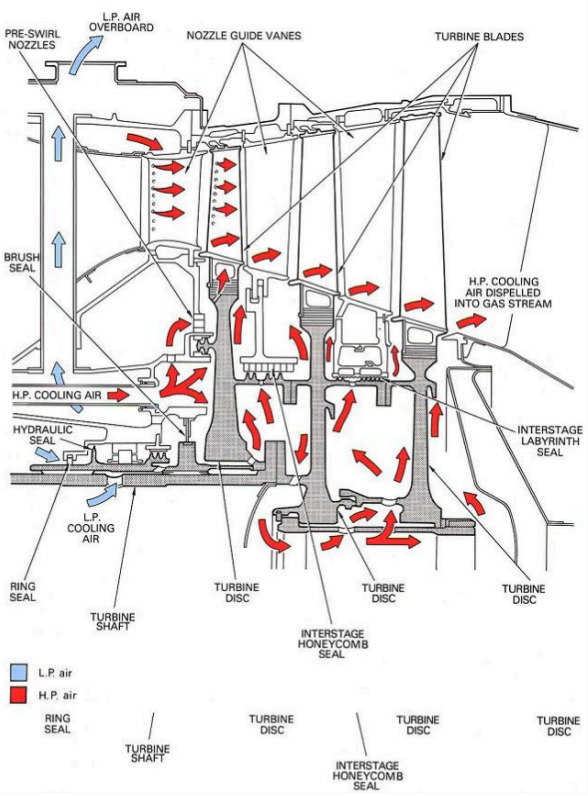

Figure 18. Turbine blades cooling design schematic [21]

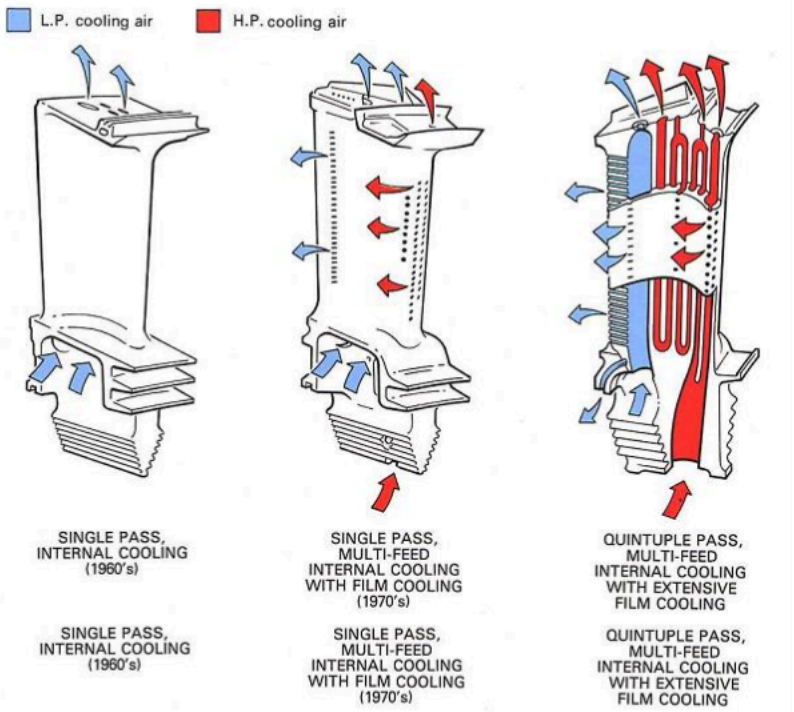

Figure 19. Turbine blades cooling design schematic [21]

It is now more than evident that methods of cooling structure heavily rely upon channeling relatively cold fluid through channels adjacent to the relatively hot structure surfaces so that plastic deformation is prevented. Preventing plastic deformation maintains the mechanism in the HCF regime, a more economic business case. This concludes the exploration of thermal management systems and how life cycles of these are determined.

Chapter 3. FSI THERMAL MODEL CFD CONFIGURATION

3.1 3D Model Geometry

The pertinent UW RDE is composed of five major components: A steel front plate, copper inner and outer cylinders, a steel outer sleeve, and a steel end plate, as shown in Figure 20.

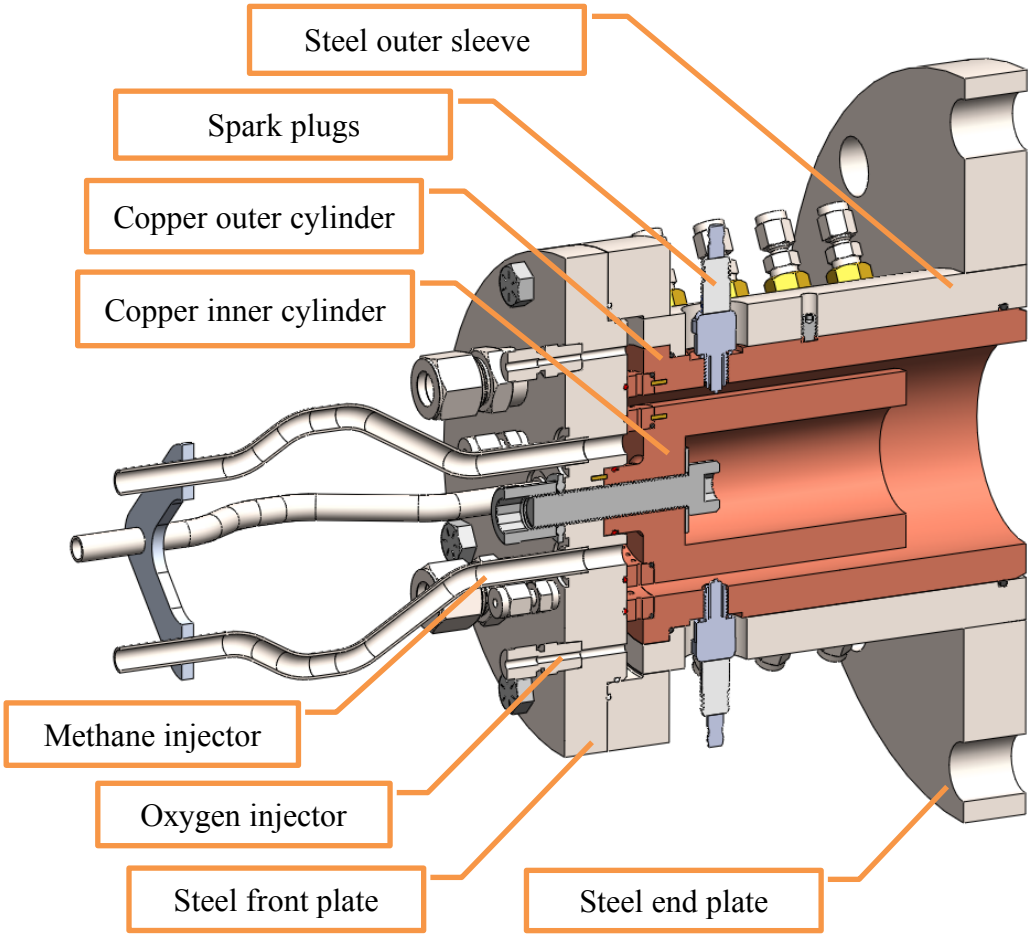

Figure 20. University of Washington RDE section cut view [11]

Additional minor components are also depicted, like fuel and oxidizer injectors, spark plugs, and pressure/temperature transducers. These will have minimal effect in the thermal efficiency of the structure when handling the detonation induced temperature spikes; therefore, these will be represented by simplified geometry within the listed five major components in the FSI model

except for the spark plug. The spark plug is being modeled as 96% aluminum oxide material to analyze possible hot spots at the protrusion edges on the outer cylinder and outer sleeve. To Correctly model the RDE with FSI capability the model must have continuous geometry in between each adjacent component. Continuous adjacent geometry is necessary for nodal information to be communicated between inside a component and between nodes within adjacent components, much like a fluid communicates information throughout a strictly CFD model. The RDE FSI model can then be thought of as a continuous solid/fluid representative geometry. To achieve this continuous geometry the 3D model first begins as one large solid providing the canvas, then the major components where designed, Boolean extracted/united, and kept within the modeling environment. This building method will be identified as a "clay cut" method.

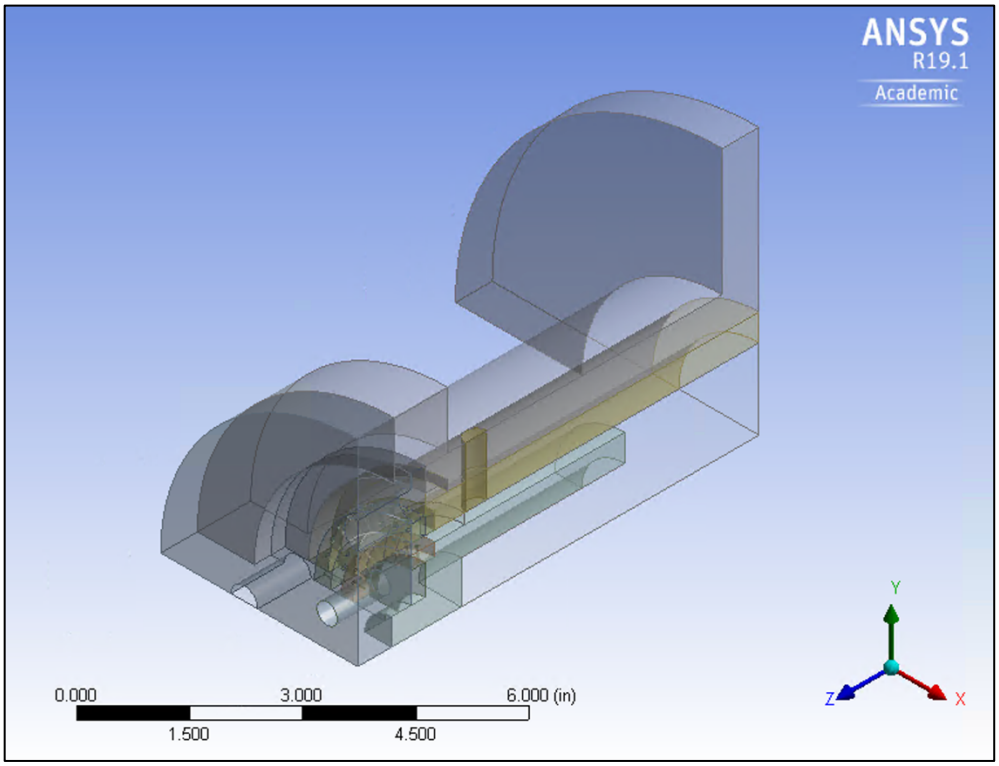

Figure 21. RDE 3D model clay building method result

Figure 22 shows the resulting 90° cut fluid geometry within the RDE geometry and Figure 23 shows a sectional view of the FSI model to be meshed, respectively.

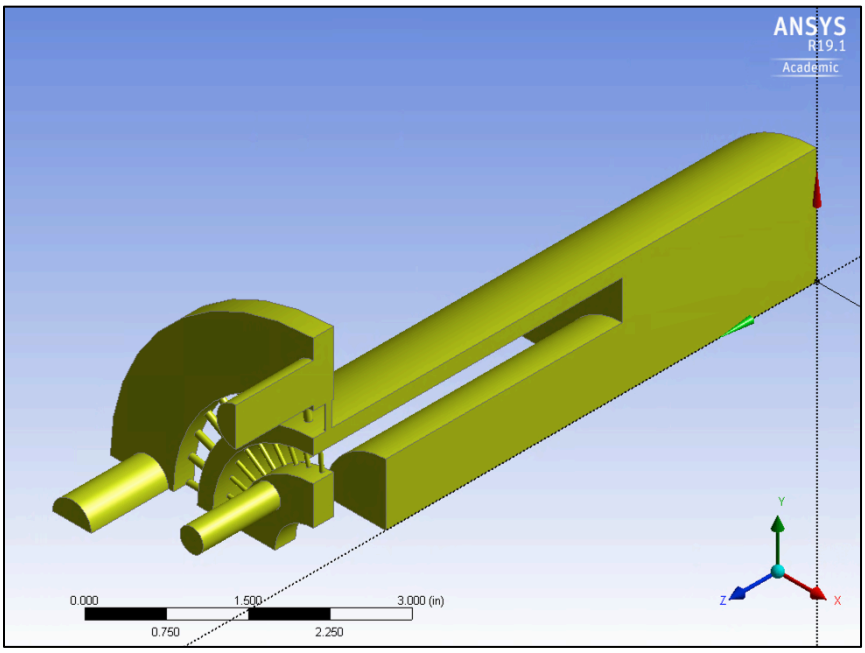

Figure 22. Resulting fluid geometry within the solid RDE geometry

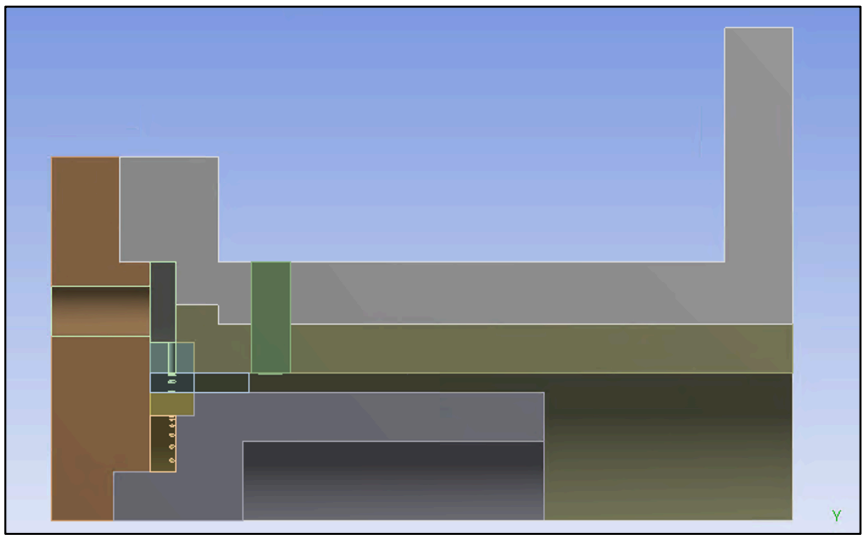

Figure 23. RDE sectional view before meshing

To keep computational expenses low and FSI model running time practical a 90° cut of the RDE model was used. With respect to oxygen and fuel injection ports and heat-transfer capable mass, the 90° cut is an ymmetric representation of the model such that the solution is representative of the 360° model.

3.2 Mesh method and Mesh Quality

An FSI model requires a physically representative CFD solution within the fluid and FEM heat transfer solution between the fluid and solid as well as between solids. The fluid portion of the model was modeled with growth rate from the non-slip walls to account for the boundary layer, as shown in Figure 24.

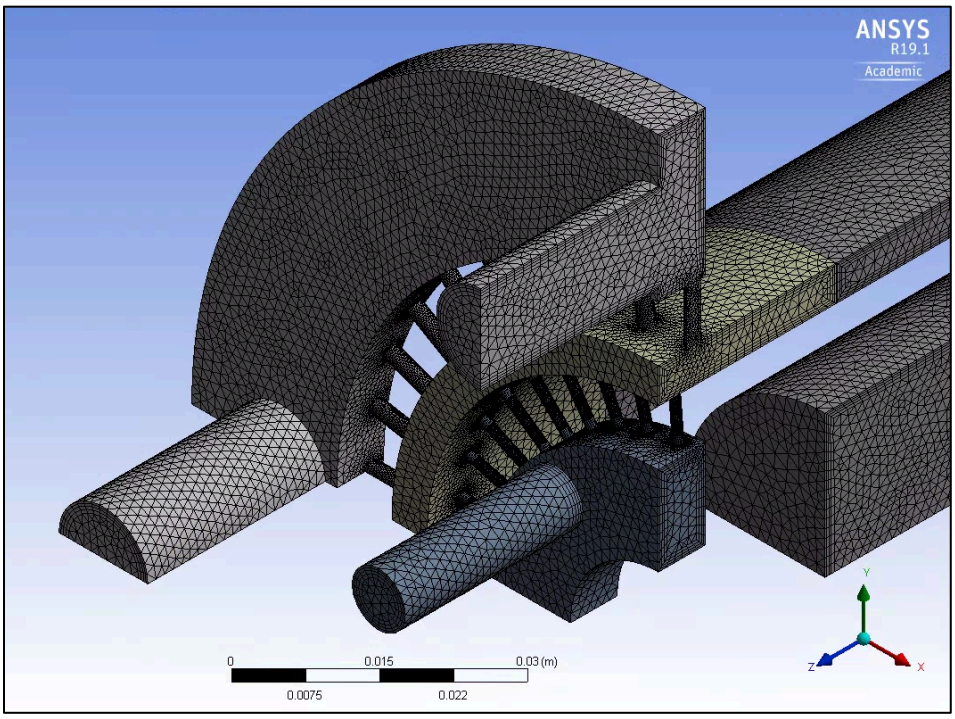

Figure 24. RDE CFD fluid plenum mesh

Smooth mesh cell size transition provides results closest to the model's physical representation. Sudden changes in mesh cell size creates errors that can be avoided with smooth cell size transition, easily achieved with a mesh growth rate implementation. A similar growth rate mesh, without layers, was implemented on the solid portions of the major solid components. Figure 25 shows the final section cut of the engine. The dark regions are shown in more detail in Figure 26, where the inflation mesh method shows the gradual increase in cell size.

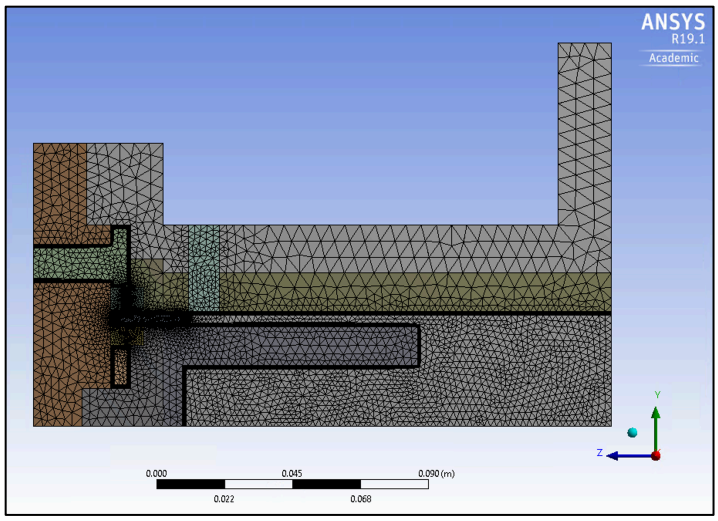

Figure 25. RDE 90° section cut mesh

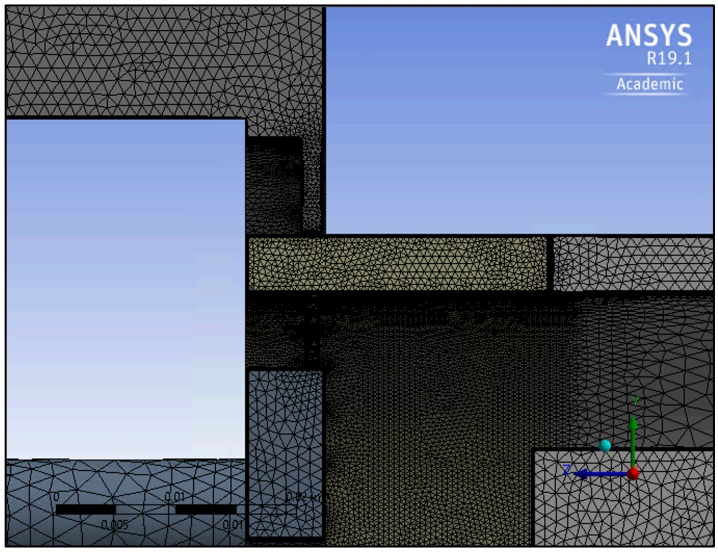

Figure 26. Partial RDE 90° section cut flow field mesh

As previously mentioned, the nodes at the surface of each of the solids and fluid plenum exist such that adjacent geometry shares the same node, allowing information to travel throughout the mesh as one full communicative entity to approximate the most the physical environment.

It is important to identify the section where the heat input will be provided to the model. As previously stated, the analysis is being made with a single-phase FSI model; therefore, a heat input will not be resulting from actual detonation but rather a volume of detonation is being placed

downstream of the fuel and oxygen injection ports. Figure 27 shows the location of the heat input volume. The axial length of the volume was determined to be approximately 0.254 m (1 in) per lab test data that showed the peak temperatures where being reached as soon as 0.254 m (1 in) 1 inch from the front plate wall [8].

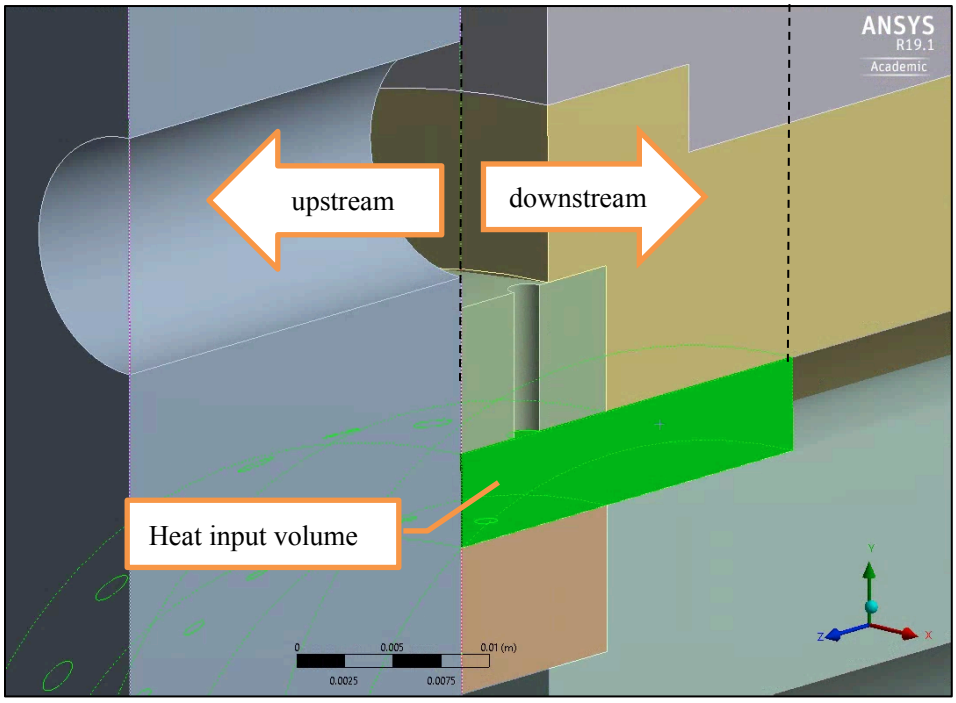

Figure 27. Heat input volume

Heat will be radiating from the plane of heat input towards positive and negative z-directions. It can be identified that the mesh is built to analyze the heat flow in this area in particular with a boundary layer growth rate by the plane on both sides of the plane. This plane will now be identified as the “detonation plane”. The plenum zone upstream of the detonation plane will be identified as the “upstream plenum” and the plenum zone downstream of the detonation plane will be identified as the “downstream plenum”. Figure 28 shows a closer look at the area.

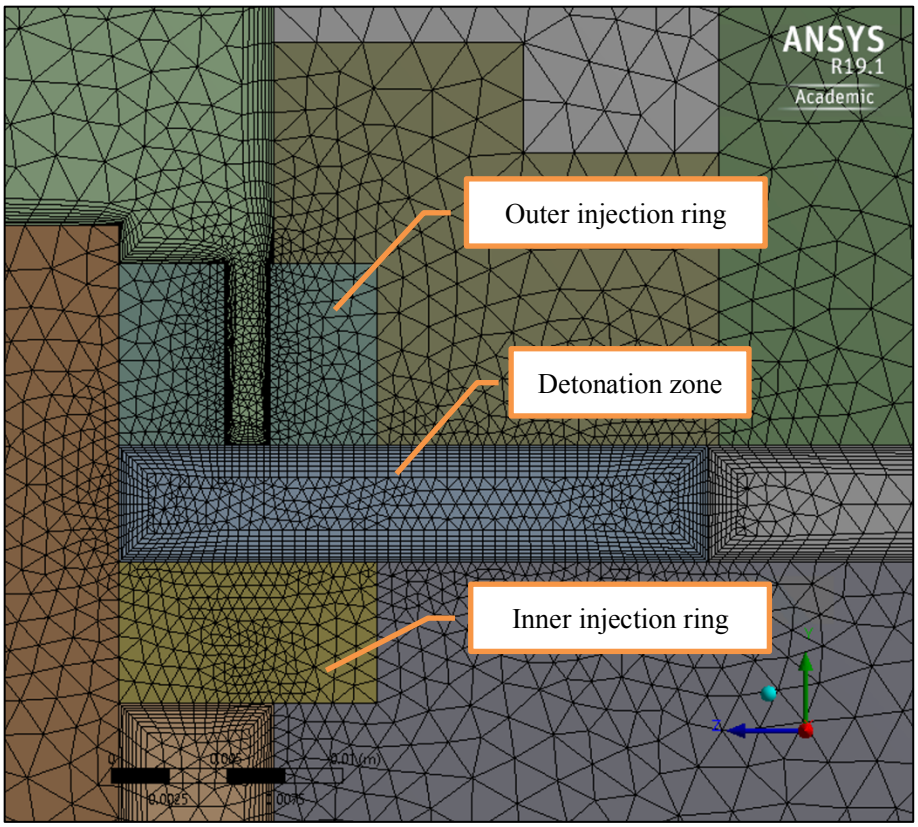

Figure 28. Detailed view of detonation plane, plenum, and surrounding solids mesh

The parameters used in the building of the mesh were kept consistent throughout the model with a few exceptions. Plenum boundary layer was consistently modeled with 12 layers and 1.15 growth rate inflation to provide the highest accuracy for the fluid solution. This guaranteed gradual cell size change and placed valuable finer cell sizes in zones where information is of the highest value, at the injection ports and at the detonation plane. Table 1 provides the statistical summary of the FSI model.

Table 1. Mesh cell size and statistical parameters

Element Size [m]	Smooth Quality	Mixing zone element size [m]	Growth rate	Nr. of Elements
1.0e-3	High	5.0e-4	1.15	3,737,371

Table 2 has the summary of the growth rate inflation as implemented through different boundaries throughout the model.

Table 2. Mesh inflation parameters

Method	1st Layer Thickness [m]	Growth Rate	Nr. of Layers
Inflation	1.0e-5	1.15	12

3.3 FLUENT MODEL CONFIGURATION & QUANTITIES REPORTS

3.3.1 *Heat Source*

The following are assumptions and boundary conditions used in the analysis with their respective reasoning. The main purpose of the analysis is to model the behavior of temperature as it dissipates through the fluid and structure; therefore, the heat input is of utmost importance. The heat input was determined to be well represented by the Lower Heating Value (LHV) of methane. Heating values are the amount of heat released during combustion. The lower LHV is the result of the total energy, Higher Heating Value (HHV), minus the heat of vaporization because the energy required to vaporize the liquid water product is not released as heat. The LHV for methane is tabulated to be 50 MJ/kg when combusted at 25C across a constant pressure field [22]; therefore, this is the

value being used as the heat source within the volume of heat input. The volume shape of the heat input is bounded by the annular area and an axial distance determined by UW RDE test data. The test data showed that the plenum is reaching peak pressures approximately 1 inch downstream of the front plate; therefore, 1 inch was used to bound the heat source input.

3.3.2 *General Solution*

The operating condition was set as 1 atm. The general solution used is pressure based. The density-based solver time step calculations are based on acoustic time scales. This requires smaller time steps which leads to higher computation costs, but eventually more accurate results. The density-based solver would be suggested once the model includes shock wave analysis. A steady solution was desired to calibrate the pressure inlets such that the Fluent correctly models a stoichiometric mixture. A steady solution also provides the steady state heat flux of the engine, flow velocity, and characteristic distance of the mixing flow. It is also useful to conduct the mesh convergence analysis. A 2^{nd} order implicit solution was chosen due to it reaching convergence faster than explicit even though it uses more memory. Thereafter, transient solution was desired to analyze the possible fluctuations of heat flow over time throughout the fluid and structure alike as well as fluctuations of velocity and turbulence mixing due to heat input.

3.3.3 *Boundary Conditions & Solvers*

Injectors were chosen to be pressures inlets which were used to calibrate a stoichiometric mass flow rate. The outlet was chosen to be a pressure outlet vent with the test setup configuration of 50662 Pa gauge. The energy input of 1.05×10^{11} was determined with methane LHV of 50 MJ/kg as a function of propellant flow rate and heat-input volume. The methane-oxygen mixture properties were kept default from the Fluent database with the following changes: The density of

the mixture was deemed as compressible ideal gas, with changes in density accounted for. The Thermal conductivity and Viscosity of the mixture both used the ideal-gas-mixing-law and the Absorption Coefficient used the wsggm-domain-based option provided by Fluent. The model uses a two-equation turbulence model k-w which models turbulent viscosity and is desired for high speeds and transonic flows. It is important to state that the SST option was included to account for turbulence induced shear stress, which is desired for wall-bounded flow. This turbulence model is not yet calibrated for multiphase analysis, so it is within the scope of the cold flow analysis being explored in this thesis. The intermittency option was chosen to help provide corrections for cross-flow as well as it is recommended by Fluent for injection models. Two-equation solvers tend to produce excessive turbulence energy in the stagnation regions by high shear strain rates, so the Kato-Launder option was chosen to limit this production by replacing the turbulence energy in these regions by a function of magnitude of vorticity, which is very small in stagnation. For radiation the Discrete Ordinates (DO) solver was implemented. This solver implements a transport equation to solve for radiation intensity in spatial coordinates. The uncoupled implementation was used, which uses a conservative finite-volume scheme, which is analogous to unstructured meshes as the one in this analysis. This implementation solves the equations for energy and radiation intensity one after the other instead of simultaneously. The free stream air temperature, the environment outside of the engine, was defined as 300K. The bodies were chosen to be opaque, which means the bodies will reflect some of the radiation and will absorb the remaining radiation on a thin layer on the surface. The absorption of the semi-translucent bodies was defined as a function of the mean-bam-length on the average dimension of the domain per the wsggm-domain-based mixture option. The strong FSI model is guaranteed with the inherent Fluent “shadow-wall” creation process. The shadow-wall is automatically created as a wall that communicates between

two solids or between fluid and solid. The shadow-wall does not need additional boundary condition specifications because Fluent calculates directly from the solution in the adjacent cells solving for both conduction and convection alike.

3.3.4 *Mesh Sensitivity Analysis*

A mesh sensitivity analysis was conducted to confirm the quality of the final chosen mesh provides results that would not vary if the mesh density improved. Two main types of meshes were explored: The Cutcell mesh and the Tetra Core mesh. Both used a boundary layer; however, the Cutcell mesh is limited in the user-defined boundary layer definition. Mesh accuracy was measured by comparing the resulting inlet flow-rates against the lab-measured inlet flow rates. The Cutcell provided more accurate results within 1000 iterations; however, once it was used over 10,000 iterations it failed at resolving the boundary layer. An additional attempt to increase the mesh size was done to resolve the boundary layer but it proved to be futile as the solver provided floating point errors. After exploring the Cutcell mesh it was learned that this mesh provides more accurate results than the Tetra Core mesh when compared to the lab boundary conditions and resulting flow rates; however, the quality of the program-defined boundary layer was not appropriate and therefore this mesh should be used for subsonic flow models if used with the ANSYS 19.1 program-defined boundary layer. Consequently, the Tetra Core mesh was chosen due to its stability due to the user-defined boundary layer opportunity over a range of mesh densities. Figures 29 and 30 show a Cutcell mesh and Tetra Core mesh respectively. Table 3 shows the results of the analysis, which shows the error when compared to the lab-measured inlet flow rates. This comparison was done as a function of turbulence flow K-w SST analysis. The model was then calibrated with pressure inlet boundary conditions that were different from the lab-

measured numbers by 9%. Thereafter, the model had to be calibrated again after the heat of combustion was added, to confirm stoichiometric flow.

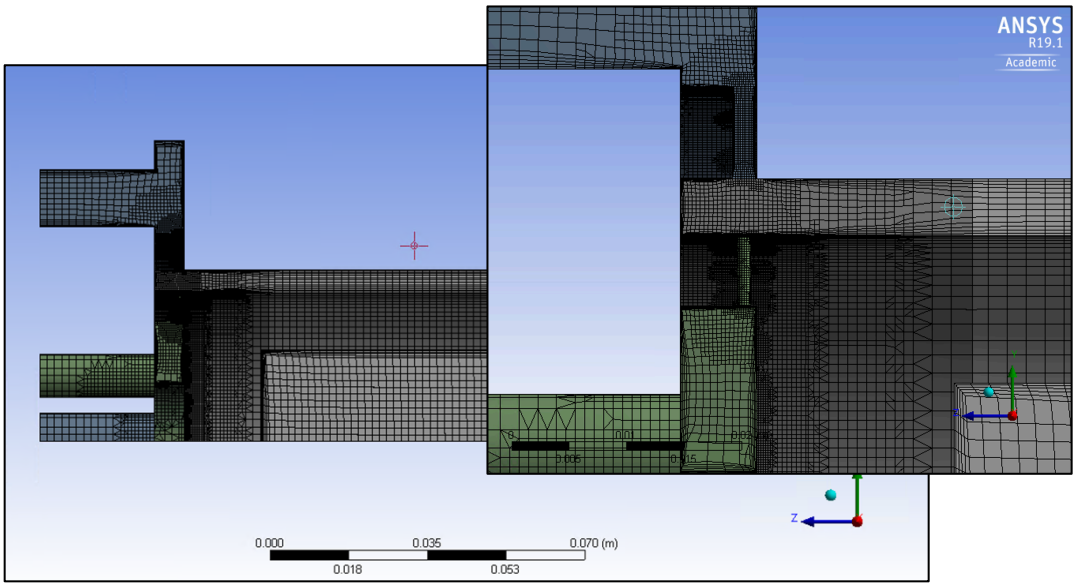

Figure 29. Cutcell mesh flow field

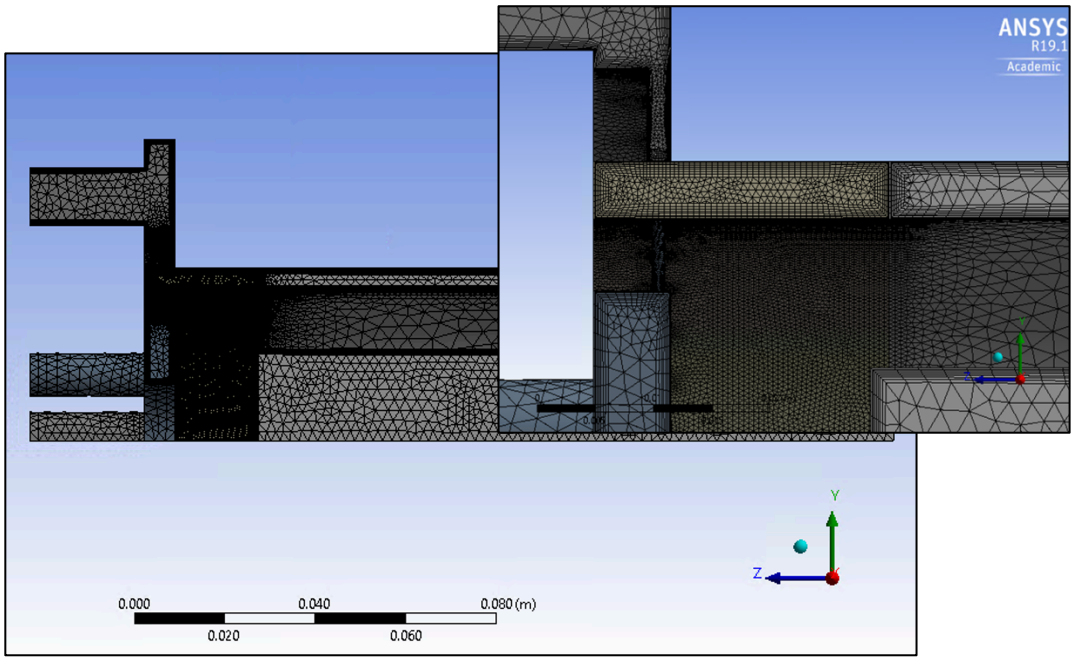

Figure 30. Tetra Core mesh flow field

Table 3. Mesh analysis results

Mesh Type	Smooth Quality	Element	N. of Elements	% Off Target
Cutcell 1	Medium	In gap 3	1,206,943	Floating point
Cutcell 2	High	In gap 6	1,214,090	Floating point
Tetra 1	Medium	0.001 m	1,991,735	30.0 %
Tetra 2	Medium	0.002 m	1,622,332	30.0 %
Tetra 3	High	0.001 m	1,992,339	30.0 %
Tetra 4	High	0.002 m	1,606,816	30.7 %
Tetra 5	High	0.003 m	1,546,065	30.0 %

Chapter 4. RESULTS AND DISCUSSION

4.1 RESULTS

4.1.1 *Turbulence Model Results & Discussion*

The turbulence model was used to confirm the stoichiometric mixing of methane and oxygen through the flow field. The model was calculated with very fine steps such that a good flow-progression was executed providing well defined steady state by 0.5 seconds. Figure 31 shows the right-side view of the velocity path lines. The helical motion of the path lines suggest mixing is occurring as the fluids flow downstream.

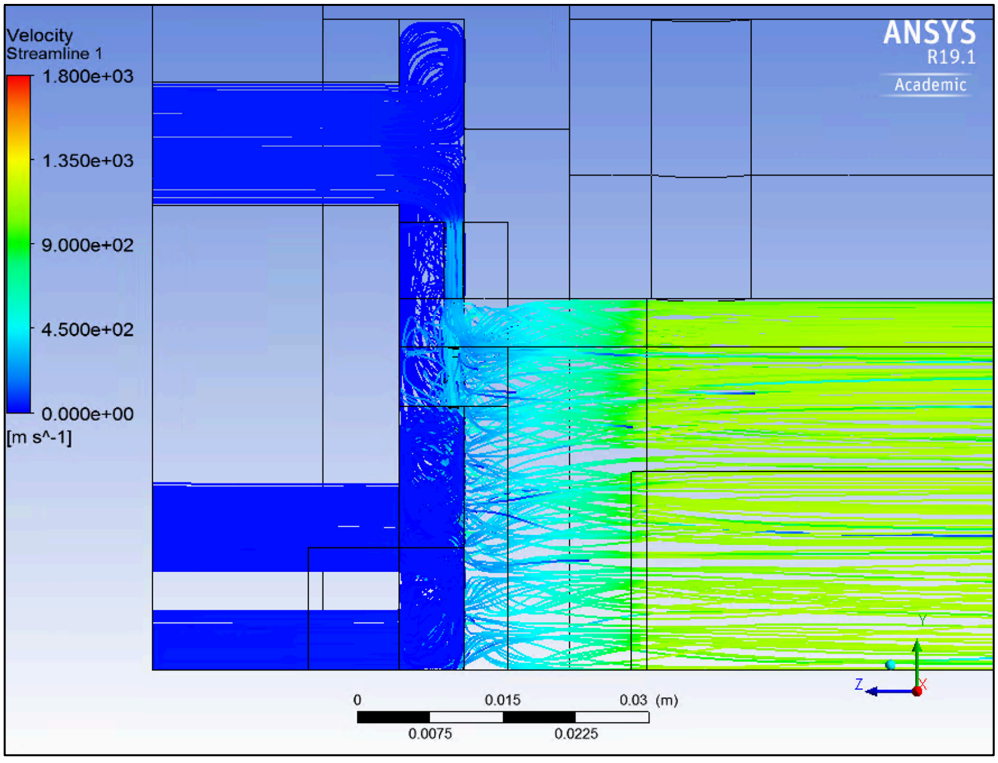

Figure 31. Right view turbulence solution at 0.5 seconds

Figure 32 shows the front view of the injection ports and mixing zone. Here the mixing can be appreciated to a higher degree. The opposite injection port directions provide a flow geometry that is highly conducive to turbulence/mixing, as guided by the annular walls.

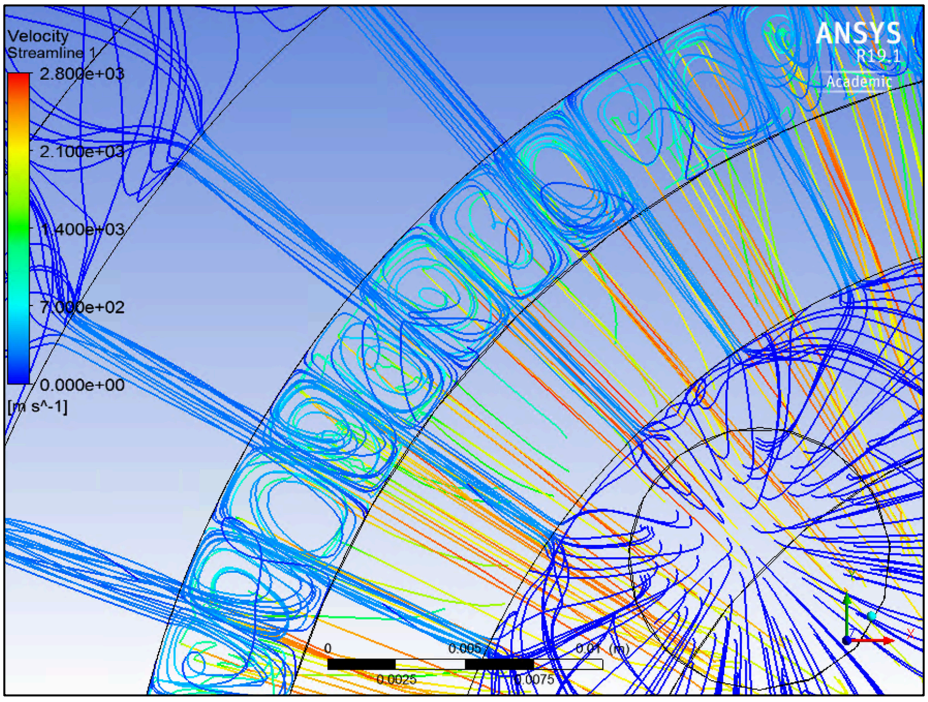

Figure 32. Front view injection ports and mixing zone at 0.5 second

This however doesn't mean the fluids are fully mixed as soon as they exit out of the injection ports and into the mixing zone. Figure 33 shows the methane mass fraction through downstream planes to show the mixing of the combined fluids as the it progresses downstream. The regions where methane mass fraction is zero is equivalent to oxygen mass fraction of one.

Each plane in this figure is offset by 0.2 in. By 0.4 in. downstream of the injection ports, the vortices can be seen forming, creating the desired mixing.

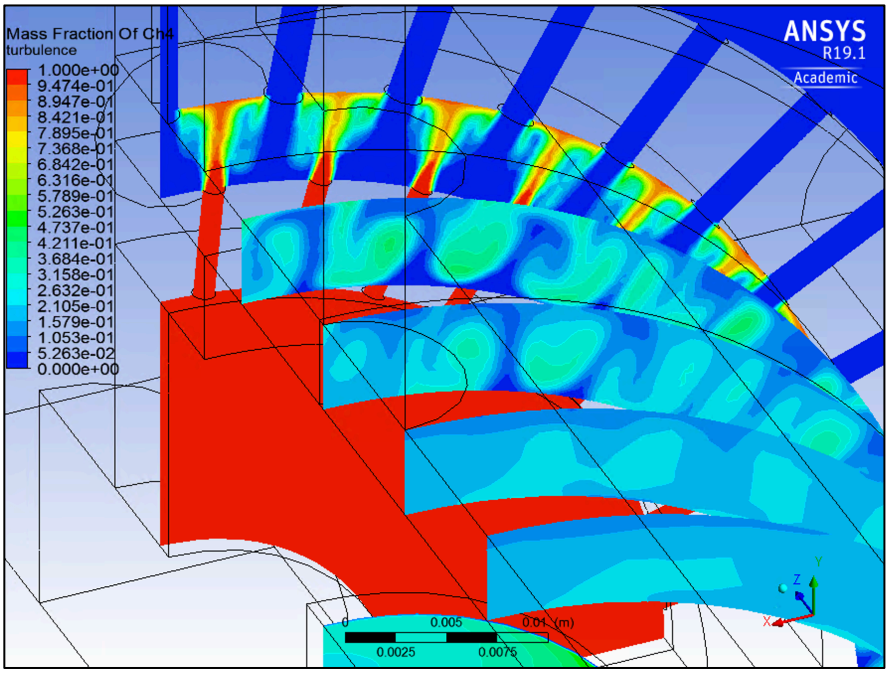

Figure 33. Methane-oxygen mixing through methane LHV heat input at 0.5 seconds

The mixing comes to full effect, creating a stoichiometric mixture, once the fluid flows approximately 0.8 – 1 in. downstream of the injection ports. A stoichiometric methane-oxygen mixture is 1 part methane and 4 parts oxygen, making methane 20% of the mixture. In the last downstream plane in Figure 33 it can be seen that the methane mass fraction is indeed 0.2, which confirms a stoichiometric mixture. This coincides with the placement of the spark plugs and the lab experimental data used to define the heat-source volume, which will be discussed further in the following section.

4.1.2 *Thermal Model Results & Discussion*

The thermal model consisted of introducing a volume in the plenum which was defined as the mixing zone. This volume provides 50 MJ/kg of energy as a heat source uniformly throughout the mixing zone. 50 MJ/kg is the LHV of the methane, which is the resulting energy after the water product of the chemical equation has fully experienced the phase change from fluid to gas. This is also where material definition is important. The inner cylinder, outer cylinder, and injection rings are made of copper due to their ability to transfer heat faster compared to the steel, which makes up the material for the front plate and outer sleeve. The spark plugs were modeled with 96% aluminum oxide ceramic for this analysis [22]. Understanding that this is not a shock-wave driven model is important to state. The thermal results are an approximation to the RDE model in the aid of structural and flow field design. Figure 34 shows the sectional view of the engine with vertical lines defining lines that were used to gather temperature profile information.

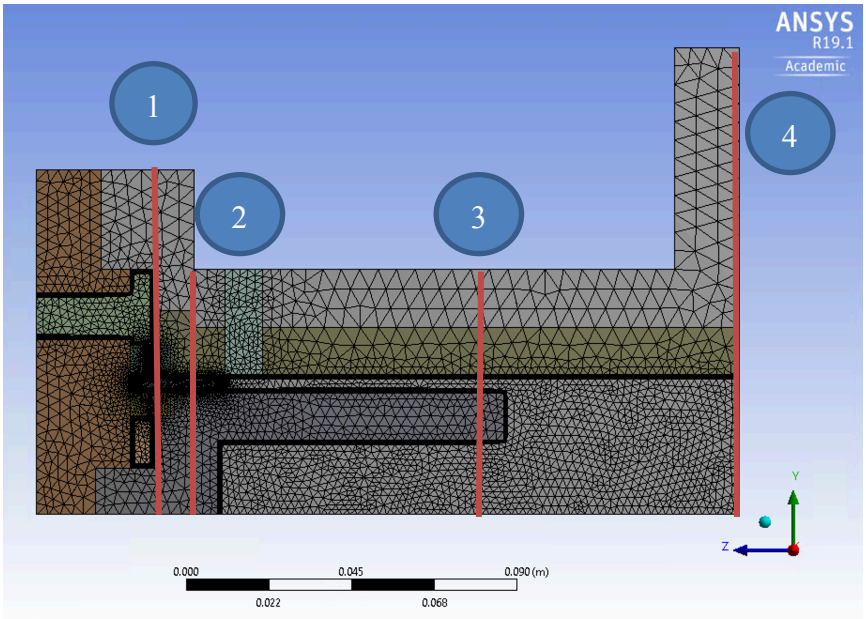

Figure 34. Lines used to gather temperature information

Line 1: Temperature profile through all engine materials (except front plate) immediately downstream of injection ports.

Line 2: Temperature profile at the heat input location.

Line 3: Temperature profile at exit of inner cylinder.

Line 4: Temperature profile at exit of engine.

Figure 35 – 38 show the resulting temperature profile after 1 second of operation for the latter to help illustrate the temperature profile against the y-axis.

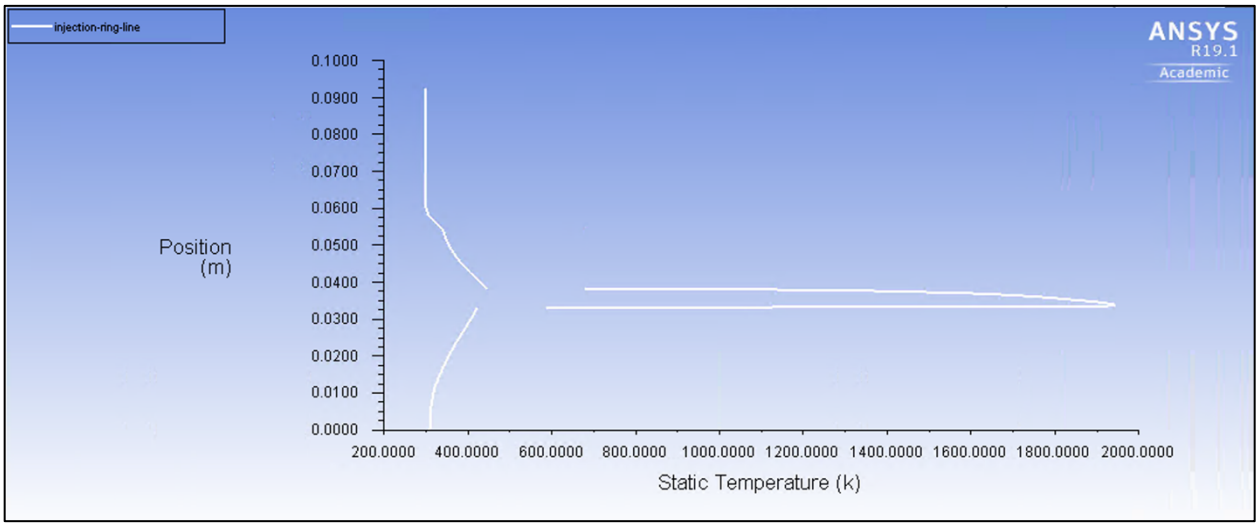

Figure 35 Line 1 Temperature profile at 1 second

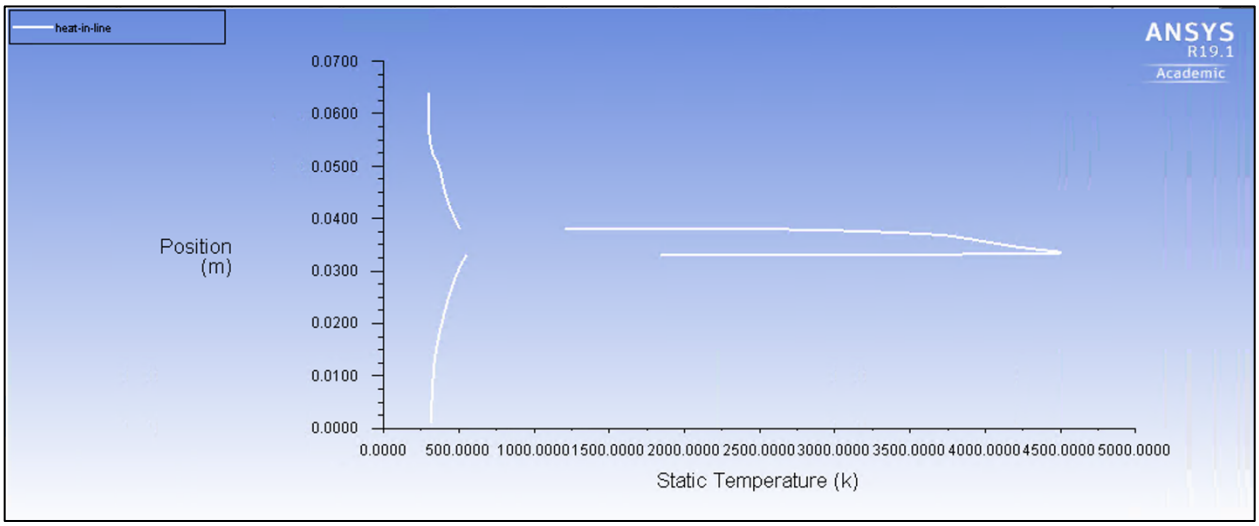

Figure 36 Line 2 Temperature profile at 1 second

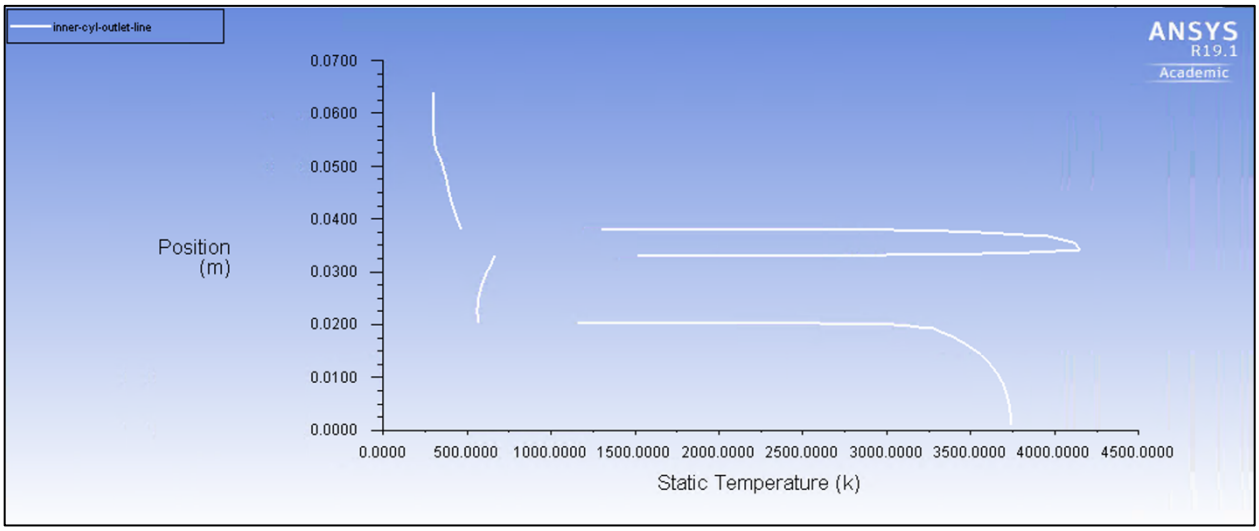

Figure 37 Line 3 Temperature profile at 1 second

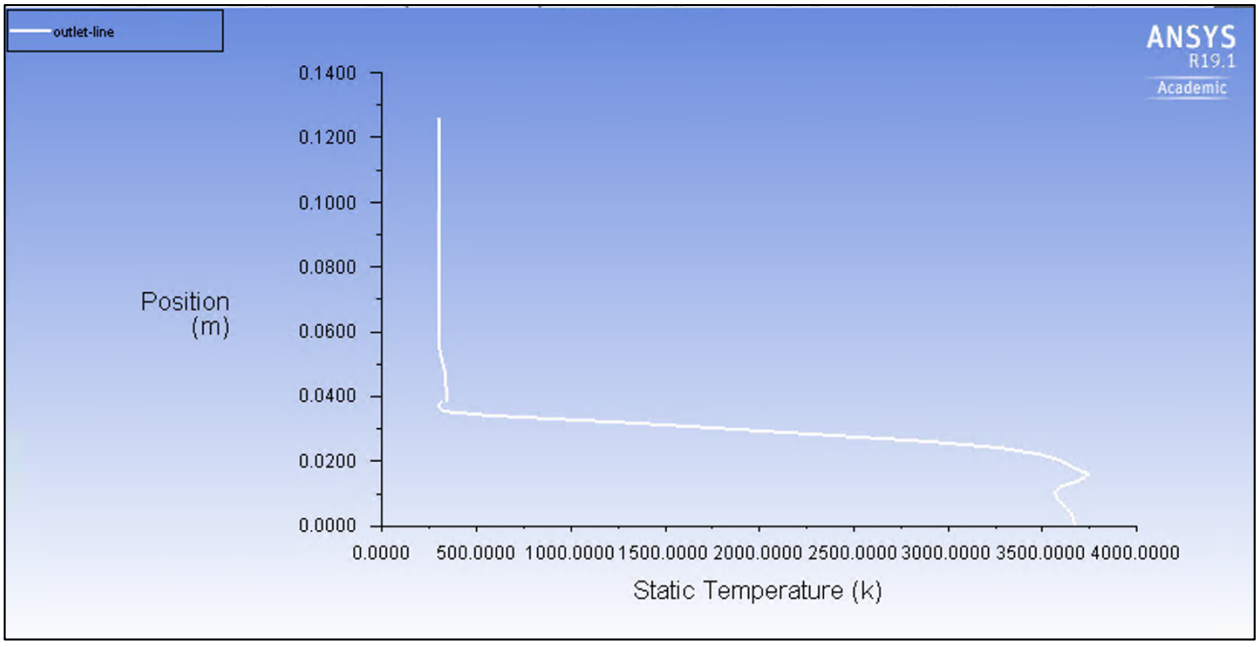

Figure 38 Line 4 Temperature profile at 1 second

Following the temperature profiles, temperature contours were gathered to determine temperature distribution and possible hot spot formation.

Comparing Figure 39 with 40, it is evident that the thermal mass advantage in the outer cylinder lie on its larger size allowing it to propagate the temperature over a larger volume. The largest temperature seen at the inner cylinder is in the order of 720K while the outer cylinder only reaches 460K after 1 second of operation. There is not much concern in the copper inner and outer cylinders for 1 run at 1 second of length time. This heat transfer is by means of convection only with the detonation zone as the energy source.

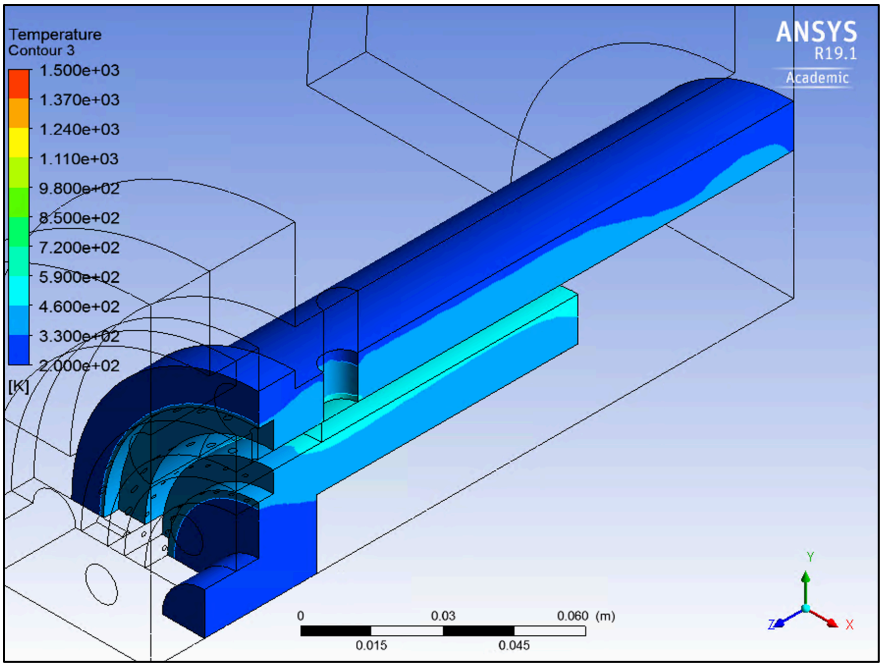

Figure 39 Inner and Outer Cylinder temperature propagation at 0.5 seconds

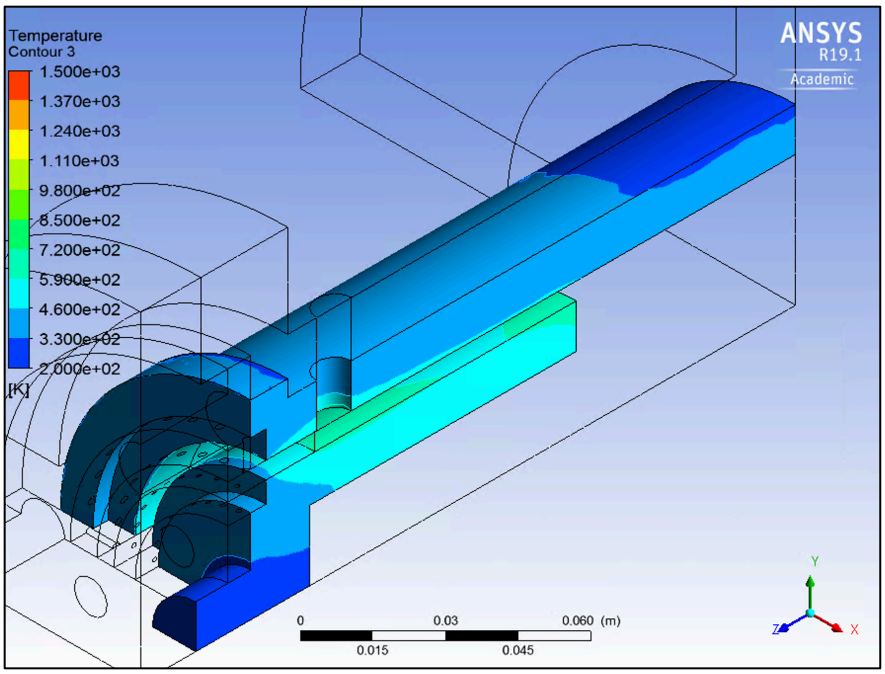

Figure 40 Inner and Outer Cylinder temperature propagation at 1 second

Comparing Figure 41 with 42, the outer sleeve sees much lower temperatures and the change in temperature is also less drastic over 1 second. As expected, hot spots are forming at the surface region closest to the detonation zone even though it is purely by means of conduction between the outer cylinder and outer sleeve. The outer sleeve temperature profile shows temperatures that resemble temperature probe readings in the lab experiments. This helps build assurance in the model's ability to predict thermal analysis results that approximate the real testing environment within +/-10K at the outer sleeve component.

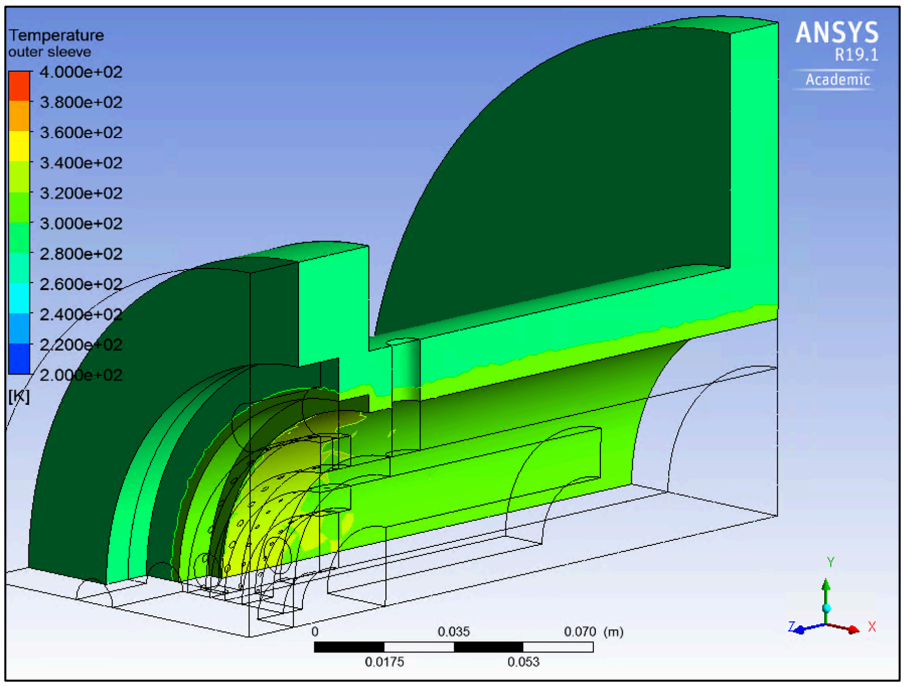

Figure 41 Outer Sleeve temperature propagation at 0.5 seconds

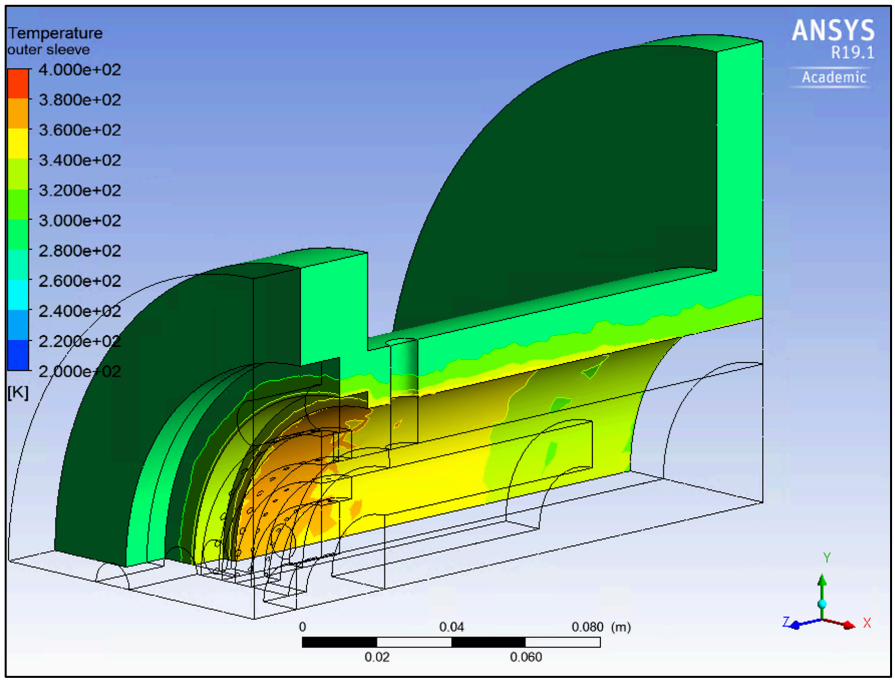

Figure 42 Outer Sleeve temperature propagation at 1 second

Comparing Figure 43 and 44, the temperature gradient is most impacted where the detonation zone and the front plate meet reaching temperatures of up to 850K. The front plate is made of steel which has a lower thermal conductivity property. This convection phenomena is interesting to compare with the conduction happening between the copper and steel in the latter two figures. The outer cylinder conducted heat into the outer sleeve steel at a lower rate than that at which the detonation zone is providing heat to the front plate by convection. The result is a hot spot of large quantities in the same period of 1 second. The propagation of heat through the front plate is also evident in the section view when comparing against the propagation of heat through the injection rings. Through 1 second the injection rings propagated the heat faster avoiding a hot spot.

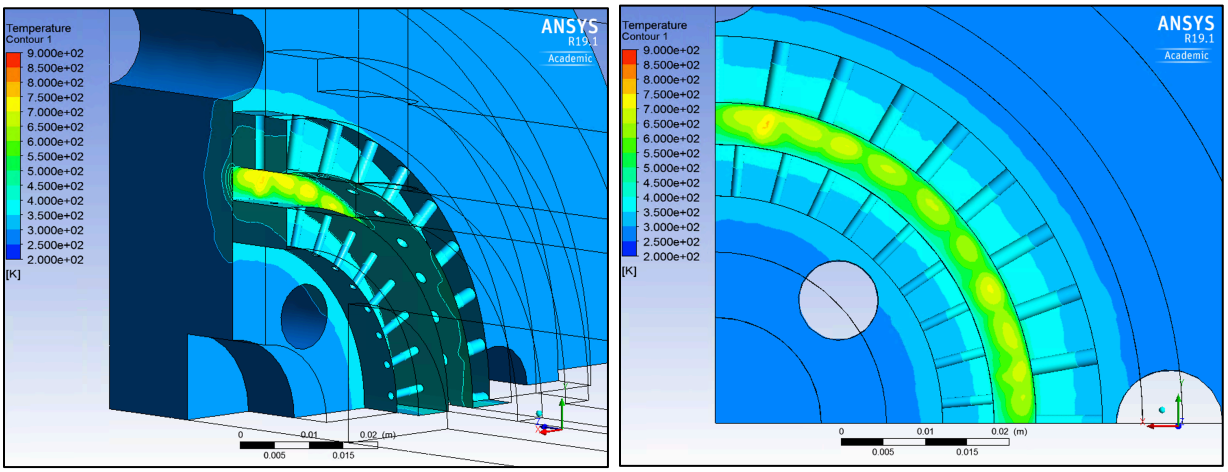

Figure 43 Front Plate and Injection Rings temperature propagation at 0.5 seconds

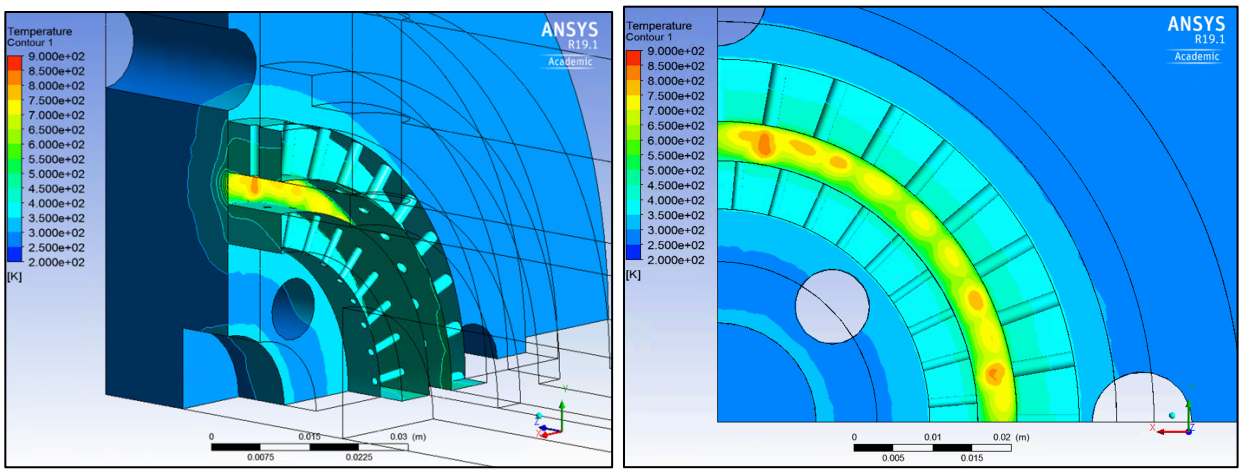

Figure 44 Front Plate and Injection Rings temperature propagation at 1 second

Last but not least, the injection rings are being compared with an interesting finding. Looking at Figure 45, the inner injection ring is experiencing a lower heat profile than the outer injection ring after 1 second, and it is by a large margin of approximately 120K.

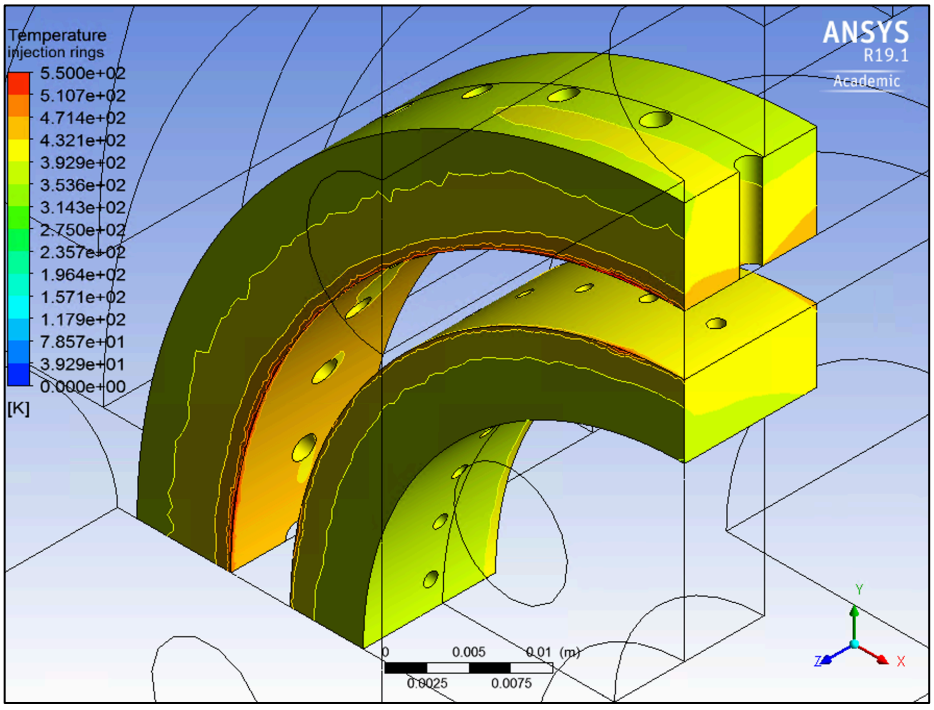

Figure 45 Inner and Outer Injection Ring temperature profile at1 second

The reasons behind this event possibly lies behind the configuration of the experiment with respect to the choice of fluid injection through the inner ports and outer ports but mostly due to the fluid thermal profile inside the inner cylinder. From the known stoichiometric injection, oxygen is being injected at 4 times the flow rate of methane. The amount of oxygen is flowing at 0.06kg/s while methane is flowing at 0.015kg/s. The outer injection ring does not experience the same benefit however. This phenomenon works in favor of the engine design. An annular engine has thermal management obstacles that are intrinsically being managed by the inherent injection port choice with oxygen, the higher mass flow rate of the two, in the outer injection plenum. Figure 46 shows a more detailed view with two contours. The left-hand side legend pertains to the mass fraction of methane in the mixing region between the two rings, while the legend on the right shows the temperature at the rings. Here it is more evident how even though the inner ring is inside, it manages to stay cooler than the outer ring.

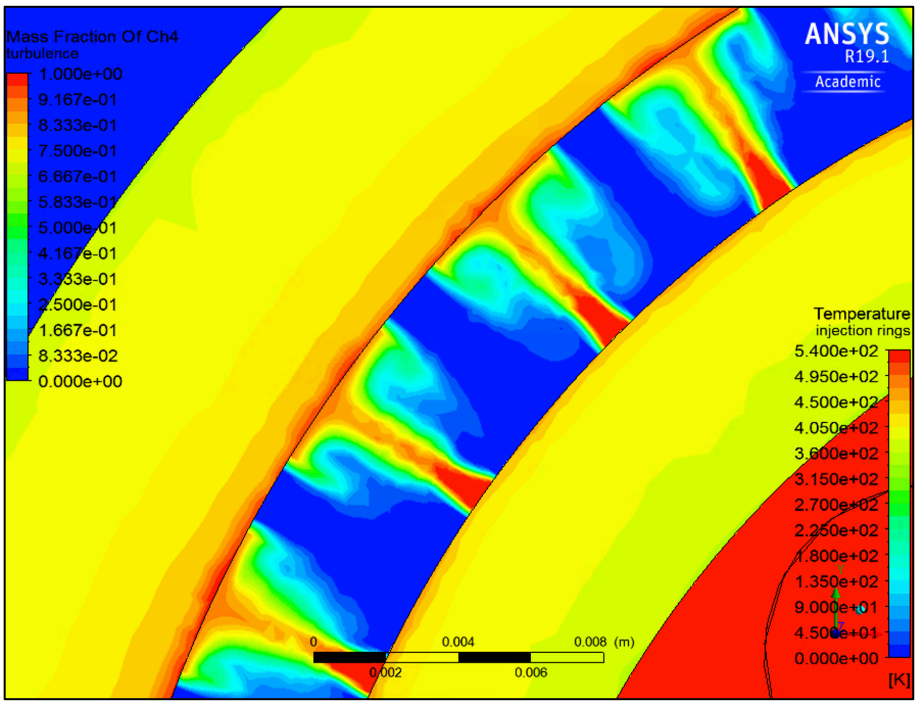

Figure 46 Inner and outer ring temperature contour & methane mass fraction contour between injection rings at 1 second

Figure 48 shows the right-side thermal contour close-up at the interaction of the fluid structure interface at 1 second where the thermal gradient can be appreciated in favor of the inner injection ring. There is a large portion of the inner injection ring section that is staying cooler than the remaining mass of both injection rings combined, outlined by the circle in Figure 48, even though heat can concentrate more towards the centerline of the engine.

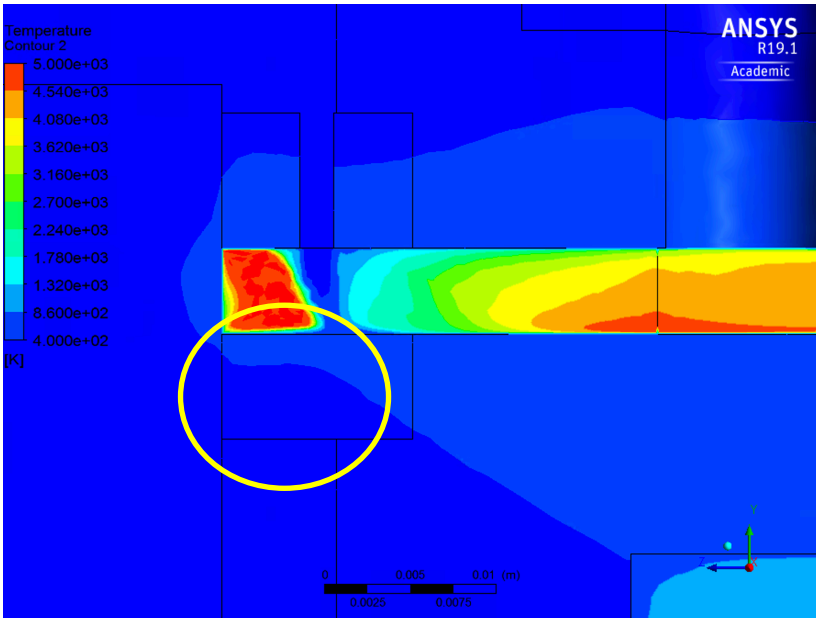

Figure 48 Thermal gradient at injection zone at 1 second

Total heat transfer data was gathered to identify the components that experience the most heat and to conduct an energy balance calculation. As already explored in the discussion of Figure 45, the front plate, inner, and outer cylinders have the highest probability of absorbing heat from the detonation zone and aft plenum, being that these are in direct contact with the heat source. Figure 47 proves that our hunch was correct for the first two components from largest temperature

experienced to lowest. The trend from highest temperature to lowest is asymptotic around 430K with respect to the front plate and inner engine components.

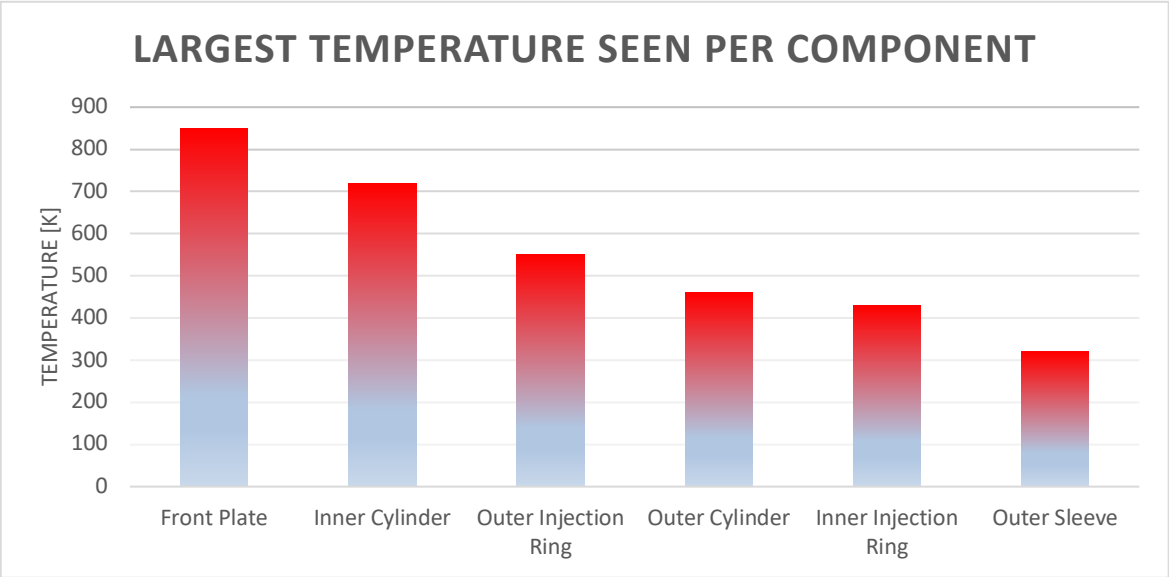

Figure 47 Largest temperature seen per component at 1 second

As already explored, we found that the inner injection ring stays cooler than the outer injection ring. However, it is surprising to notice that the inner injection ring also stays cooler than the outer cylinder. Once again, when comparing all components, he larger mass flow rate being injected from the outer portion of the plenum injection is showing benefits. One additional comparison can be appreciated when paying attention to the two components that see the least heat. Before the model produced results, one perfectly fine hypothesis is that the inner injection ring is going to be hotter than the outer sleeve after a 1 second run. However, to realize that these two components experience the least temperature even though they are the most interior and most exterior components is remarkable.

Table 4 shows the energy balance breakdown. Most of the energy is being expelled out through the outlet. The ceramic spark plug has not been mentioned much due to the fact that ceramic does not conduct significant heat; nevertheless, the ceramic heat flux is accounted under the Heat to Walls in Table 4 [22].

Table 4 Energy Balance

Inlet	Heat in	=	Outlet	Heat to Walls	Heat to Radiation
128.15 W	0.75×10^6 W		636,048.7 W	113,760 W	22.22 W

Lastly, radiation results were gathered over the 1 second amounting to 22.22 W of heat radiated out of the system. Radiation surfaces were composed of the front plate, outer sleeve, and the downstream surface of the outer cylinder. As expected, radiation over 1 second of operation was minimal and therefore was of small consequence for the model.

Chapter 5. CONCLUSION AND RECOMMENDATIONS

5.1 CONCLUSION

Thermal effects from Methane-Oxygen stoichiometric simulated heat of combustion in a turbulent annular rotating detonation engine (RDE) have been found to be manageable without the need of thermal management supporting subsystems through a 1 second short pulse run. The RDE design successfully manages temperature spikes through highly thermally conducive copper material through the inner and outer cylinders as well as the injections rings. Hot spots were observed mainly in the front wall region adjacent to the detonation zone. The larger oxygen mass flow rate being injected from the outer ports provide a thermal management benefit by creating impingement on the inner injection ring, making the inner injection ring the second coldest component in the engine. The impingement consequently provides thermal relief to the inner cylinder as well. The front plate and inner cylinder experience the highest temperature while the outer sleeve and inner injection ring experience the least temperature, even though the outer sleeve is farthest from the engine's center line and the inner injection ring is positioned in what could have been hypothesized as the hottest region in the engine.

5.2 RECOMMENDATION

Next analysis should include a shock tube detonation model as a proven base to develop a shockwave RDE model. Multiple software, including ANSYS, provide the opportunity to input spark location, spark energy, spark time, and duration which allows for fast model development in a multiphase model. Calibration of a multiphase model will require research and analysis of the chosen mixture's activation energy and heat of reaction variables. Further thermal analysis should include a thermal fatigue analysis to determine the RDE life cycle; however, further thermal analysis will serve as an approximation due to the lack of shockwave presence in the model. A water jacket/film cooling system should be created after a thermal fatigue analysis is completed. It is recommended that a maintenance schedule be created for the engine with this thesis as a portion of its basis, knowing which components are experiencing the highest temperatures in conjunction with material properties. A fatigue thermal model will help identify the maintenance schedules as well as improving the engine design and material choice. Future RDE test beds, and possibly commercially produced, should be mostly composed of copper or more thermally conducive material.

BIBLIOGRAPHY

[1] Heiser, William H., and David T. Pratt. “Thermodynamic Cycle Analysis of Pulse Detonation Engines.” Journal of Propulsion and Power, vol. 18, no. 1, 2002, pp. 68–76., doi:10.2514/2.5899.

[2] Dong, Fei, et al. “Simulation on Thermal-Stress-Fatigue of an Engine Exhaust Manifold.” SAE Technical Paper Series, 2009, doi:10.4271/2009-01-0409.

[3] Braun, James, et al. “Numerical Assessment of the Convective Heat Transfer in Rotating Detonation Combustors Using a Reduced-Order Model.” Applied Sciences, vol. 8, no. 6, 2018, p. 893., doi:10.3390/app8060893.

[4] James Koch Detonation Theory, University of Washington, 2017

[5] Fickett, Wildon Davis, William C.. (2000). Detonation - Theory and Experiment - 2.1.1 Conservation Laws. Dover Publications. Retrieved from https://app.knovel.com/hotlink/pdf/id:kt011D12M2/detonation-theory-experiment/conservation-laws

[6] Boening, J.A., “Initiation of Orderly Spinning Detonation Waves via Phased Sparking,” MS Thesis, University of Washington, 2016.

[7] Washington, M.R., "Radial Injector Mixing Effects on Detonation Zone Position in Rotating Detonation Engine," MS Thesis, University of Washington, 2019

[8] Fievisohn, Robert T., and Kenneth H. Yu. “Steady-State Analysis of Rotating Detonation Engine Flowfields with the Method of Characteristics.” Journal of Propulsion and Power, vol. 33, no. 1, 2017, pp. 89–99., doi:10.2514/1.b36103.

[9] Nordeen, Craig A., "Thermodynamics of a Rotating Detonation Engine" (2013). Doctoral Dissertations. 277. http://digitalcommons.uconn.edu/dissertations/277

[10] James Koch Rotation Detonation Engine Design, University of Washington, 2018

[11] Özisik M. N. Heat Conduction. 2nd ed., Wiley, 1993, sharif.ir/~moosavi/Ozisik%20Heat%20Conduction%20(ISBN%200471532568).pdf.

[12] Chen, Wenzhe Liu, Xingjun Dai, Pinqiang Chen, Yonglu Jiang, Zhengyi. (2012). Advanced Composite Materials, Part 1 - 43.4.1 Model of the Exhaust Manifold. Trans Tech Publications Ltd. Retrieved from https://app.knovel.com/hotlink/pdf/id:kt011D65W1/advanced-composite-materials/model-exhaust-manifold

[13] Renard, Arnaud. “FLUENT 6.3 Validation Guide.” FLUENT 6.3 Validation Guide, Centre De Calcul De Champagne-Ardenne ROMEO, 2006, romeo.univ-reims.fr/documents/fluent/fluentValidationGuide.pdf.

[14] Schwer, Douglas, and Kailas Kailasanath. “Numerical Investigation of Rotating Detonation Engines.” 46th AIAA/ASME/SAE/ASEE Joint Propulsion Conference & Exhibit, 2010, doi:10.2514/6.2010-6880.

[15] Boening, J. A., Heath, J. D., Byrd, T.J., Koch, J. V., Mattick, A. T., Breidenthal. R. E., Knowlen, C., and Kurosaka, M., "Design and Experiments of a Continuous Rotating Detonation Engine: Wave Generator and Modulated Fuel-Oxidizer Mixing," AIAA 2016-4966.

[16] Spakovszky, Z S. “Conductive Heat Transfer.” 17. Convective Heat Transfer, Mathematics Department, Macquarie University, Sydney, 1999, web.mit.edu/16.unified/www/FALL/thermodynamics/notes/node121.html#17632.

[17] “Turbulence Modeling Resource.” Edited by Christopher Rumsey, NASA, NASA, 2003, turbmodels.larc.nasa.gov/langtrymenter_4eqn.html.

[18] Pizzarelli, M., "Modeling of Cooling Channel Flow in Liquid-Propellant Rocket Engines," PhD Thesis, Universita` degli Studi di Roma “La Sapienza”, 2006/2007

[19] Asraff, A. K., et al. “Stress Analysis & Life Prediction of a Cryogenic Rocket Engine Thrust Chamber Considering Low Cycle Fatigue, Creep and Thermal Ratchetting.” Transactions of the Indian Institute of Metals, vol. 63, no. 2-3, 2010, pp. 601–606., doi:10.1007/s12666-010-0089-7.

[20] Groh, Rainer G. “Jet Engine Design: Turbine Cooling.” Aerospace Engineering Blog, 24 July 2018, aerospaceengineeringblog.com/turbine-cooling/.

[21] Nikolaidis, Pavlos, and Andreas Poullikkas. “A Comparative Overview of Hydrogen Production Processes.” *Renewable and Sustainable Energy Reviews*, vol. 67, Jan. 2017, pp. 597–611., doi:10.1016/j.rser.2016.09.044.

[22] Accuratus. “Aluminum Oxide, Al2O3 Ceramic Properties.” Aluminum Oxide | Al2O3 Material Properties, 2013, www.accuratus.com/alumox.html.

This page was intentionally left blank

VITA

Daniel Mendez is originally from Medellin, Colombia. He always wanted to be an astronaut but his father being a realistic and loving mentor explained the difficulty in such a goal. Daniel and his family emigrated to the United States in the year 2000 while he was the age of 11. There he graduated from the University of Central Florida with a Bachelor's in Aerospace Engineering and Minor in Business Management in 2012. He was granted recommendation by the chairs of the defense board to graduate with a Master of Science in Aeronautics and Astronautics with concentration in Fluids and Thesis from the University of Washington in 2019. Daniel now at 31 years of age sees that he is closer to the astronaut goal than 11-year-old Daniel would have ever thought possible. May the pursuit of dreams continue while improving human connections and making the world a better place through science, creativity, and the enduring thought of well-being for all.